

# A TRIDENT SCHOLAR PROJECT REPORT

NO. 260

---

IMPROVED TURBINE BLADE COOLING USING  
ENDWALL FLOW MODIFICATIONS

---



UNITED STATES NAVAL ACADEMY  
ANNAPOLIS, MARYLAND

This document has been approved for public  
release and sale; its distribution is unlimited.

20000424 148

# REPORT DOCUMENTATION PAGE

Form Approved  
OMB No. 074-0188

Public reporting burden for this collection of information is estimated to average 1 hour per response, including the time for reviewing instructions, searching existing data sources, gathering and maintaining the data needed, and completing and reviewing the collection of information. Send comments regarding this burden estimate or any other aspect of the collection of information, including suggestions for reducing this burden to Washington Headquarters Services, Directorate for Information Operations and Reports, 1215 Jefferson Davis Highway, Suite 1204, Arlington, VA 22202-4302, and to the Office of Management and Budget, Paperwork Reduction Project (0704-0188), Washington, DC 20503.

|   |  |   |  |  |
|---|--|---|--|--|
| 1. AGENCY USE ONLY (Leave blank)  |  | 2. REPORT DATE<br>5 May 1999            | 3. REPORT TYPE AND DATE COVERED  |  |
| 4. TITLE AND SUBTITLE<br>Improved turbine blade cooling using endwall flow modifications  |  |   | 5. FUNDING NUMBERS   |  |
| 6. AUTHOR(S)<br>Aunapu, Nicole V.   |  |   |  |  |
| 7. PERFORMING ORGANIZATION NAME(S) AND ADDRESS(ES)<br>U.S. Naval Academy<br>Annapolis, MD   |  |   | 8. PERFORMING ORGANIZATION REPORT NUMBER<br>USNA Trident Scholar project report no. 260 (1999) |  |
| 9. SPONSORING/MONITORING AGENCY NAME(S) AND ADDRESS(ES)   |  |   | 10. SPONSORING/MONITORING AGENCY REPORT NUMBER   |  |
| 11. SUPPLEMENTARY NOTES<br>Accepted by the U.S. Trident Scholar Committee   |  |   |  |  |
| 12a. DISTRIBUTION/AVAILABILITY STATEMENT<br>This document has been approved for public release; its distribution is UNLIMITED.  |  |   | 12b. DISTRIBUTION CODE   |  |
| 13. ABSTRACT: A flow modification technique designed to allow increased turbine inlet temperatures while keeping the turbine blades below their thermal limits is introduced. A large-scale two-half-blade cascade simulator is used to model the secondary flow between two adjacent turbine blades. Various flow visualization techniques and measurements are used to verify that the test section replicates the flow of an actual turbine engine. Two techniques are employed to modify the endwall secondary flow by altering the flow characteristics, specifically the path of the horseshoe vortex. Fire wall jets are installed at a location downstream of the saddle point near the leading edge of the pressure side blade. These wall jets, near the saddle point, are found to be ineffective in diverting the path of the horseshoe vortex. The second technique utilizes a row of 12 centerline wall jets whose positions are based on results from a modified fence. The row of jets have successfully diverted the path of the horseshoe vortex and decreased its effect on the suction side blade. This can be expected to increase the effectiveness of film cooling in that area. However, the row of jets increased the aerodynamic losses in the turbine passage, which would result in a decrease of turbine efficiency. |  |   |  |  |
| 14. SUBJECT TERMS<br>film cooling, gas turbine engine, horseshoe vortex, secondary flow   |  |   | 15. NUMBER OF PAGES  |  |
|   |  |   | 16. PRICE CODE   |  |
| 17. SECURITY CLASSIFICATION OF REPORT   | 18. SECURITY CLASSIFICATION OF THIS PAGE | 19. SECURITY CLASSIFICATION OF ABSTRACT | 20. LIMITATION OF ABSTRACT   |  |

**IMPROVED TURBINE BLADE COOLING USING  
ENDWALL FLOW MODIFICATIONS**

by

Midshipman Nicole V. Aunapu, Class of 1999  
United States Naval Academy  
Annapolis, Maryland

*Nicole Aunapu*

---

Certification of Advisers Approval

Associate Professor Karen Flack  
Department of Mechanical Engineering

*Karen A. Flack*

---

*May 5, 1999*

---

Assistant Professor Ralph Volino  
Department of Mechanical Engineering

*Ralph Volino*

---

*May 5, 1999*

---

Acceptance for the Trident Scholar Committee

Professor Joyce E. Shade  
Chair, Trident Scholar Committee

*J. E. Shade*

---

*5 May 1999*

---

## **ABSTRACT**

---

A flow modification technique designed to allow increased turbine inlet temperatures while keeping the turbine blades below their thermal limits is introduced. A large-scale two-half-blade cascade simulator is used to model the secondary flow between two adjacent turbine blades. Various flow visualization techniques and measurements are used to verify that the test section replicates the flow of an actual turbine engine. Two techniques are employed to modify the endwall secondary flow by altering the flow characteristics, specifically the path of the horseshoe vortex.

Five wall jets are installed at a location downstream of the saddle point near the leading edge of the pressure side blade. These wall jets, near the saddle point, are found to be ineffective in diverting the path of the horseshoe vortex.

The second technique utilizes a row of 12 centerline wall jets whose positions are based on results from a modified fence. The row of jets have successfully diverted the path of the horseshoe vortex and decreased its effect on the suction side blade. This can be expected to increase the effectiveness of film cooling in that area. However, the row of jets increased the aerodynamic losses in the turbine passage, which would result in a decrease of turbine efficiency.

## **KEY WORDS**

---

Film Cooling, Gas Turbine Engine, Horseshoe Vortex, Secondary Flow

## NOMENCLATURE

---

|                 |  |
|-----------------|--|
| A, B            | constants depending on fluid and type of sensor; functions of thermal conductivity, viscosity and Prandtl number |
| C               | chord (in)   |
| $C_{p_t}$       | total pressure coefficient   |
| E               | bridge voltage   |
| H               | span   |
| $H_p$           | pressure side leg of horseshoe vortex  |
| $H_s$           | suction side leg of horseshoe vortex   |
| n               | exponent (close to 2)  |
| P               | pitch  |
| $P_s$           | static pressure  |
| $P_t$           | total pressure   |
| $P_{tr}$        | total pressure in freestream upstream of the cascade   |
| P.W.            | pressure wall  |
| R               | operating resistance of the sensor   |
| $R_3$           | resistor in series with the sensor (usually 10 ohms)   |
| Re              | Reynolds number  |
| $Re_c$          | Reynolds number based on test section chord length   |
| $Re_1$          | Reynolds number based on test section inlet velocity   |
| $Re_2$          | Reynolds number based on test section exit velocity  |
| $Re_{\delta_2}$ | Reynolds number based on test section momentum thickness   |
| S.W.            | suction wall   |
| $S_p$           | concave side curvilinear distance from the stagnation line of the test blade                                     |
| $S_s$           | convex side curvilinear distance from the stagnation line of the test blade                                      |
| T               | temperature ( $^{\circ}\text{C}$ )   |
| $t_s$           | operating temperature of the sensor  |
| $t_e$           | fluid or environmental temperature   |
| U               | velocity (m/s)   |
| $U_L$           | curvilinear freestream velocity in blade passage (m/s),<br>$U_L = \sqrt{\frac{2}{\rho} * (P_{tr} - P_s)}$        |
| $U_1$           | inlet velocity (m/s)   |
| $U_2$           | exit velocity (m/s)  |
| V               | velocity   |
| f               | frequency of the Doppler shift (Hz)  |
| $\delta$        | distance between interference fringes (nm)   |
| $\delta_2$      | momentum thickness   |
| $\rho$          | density of the gas or liquid   |

## LIST OF FIGURES

---

- Fig. 1            Picture of a Gas Turbine Engine.
- Fig. 2            Gas Turbine Schematic.
- Fig. 3            Turbine blade and endwall configuration.
- Fig. 4            Terminology associated with turbine passage.
- Fig. 5            Schematic of the horseshoe vortex as it impinges the suction side blade  
(Chen and Goldstein 1991).
- Fig. 6            Endwall three-dimensional separation after Langston (1977).
- Fig. 7            Top view of Chung's test section (Chung 1992).
- Fig. 8            Endwall secondary flow in a turbine cascade (Chung, Simon and  
Buddhavarapu 1991).
- Fig. 9            Schematic of wind tunnel and test section.
- Fig. 10           Schematic of turbulence generator (Stoddard 1998).
- Fig. 11           Top view of test section.
- Fig. 12           Blade profile dimension definitions (Chung 1992).
- Fig. 13           Schematic of single tuft probe (Chung 1992).
- Fig. 14           Schematic of twirling tuft probe.
- Fig. 15           Normalized velocity distribution along the blade surface ( $Re=232000$ ).
- Fig. 16           Endwall ink dots CHUNG - saddle point.
- Fig. 17           Endwall ink dots PRESENT - saddle point.
- Fig. 18           Oil and blackpowder PRESENT - saddle point.
- Fig. 19           Endwall ink dots CHUNG.
- Fig. 20           Endwall ink dots PRESENT.
- Fig. 21           Oil and blackpowder CHUNG vs Oil and blackpowder PRESENT.
- Fig. 22           Blade ink dots (no jets).
- Fig. 23           Horseshoe vortex with and without fence (Chung, Simon, and  
Buddhavarapu 1991).
- Fig. 24           Top view of test section with wall jets near the saddle point.
- Fig. 25           Blade ink dots (near saddle pt, full fence, 2,3,4,5,6,7,8 and 3,4,5,6,7,8).
- Fig. 26           Blade ink dots (with 4,5,6,7,8 & 1,2,3,4,5,6,7 & 1,2,3,4,5,6 & 1,2,3,4,5).
- Fig. 27           Blade ink dots (with 3,4,5,6 & 3,4,5,6 (modified orientation)).
- Fig. 28           Top view of test section with modified fence in place.
- Fig. 29           Top view of test section with twelve wall jets installed.
- Fig. 30           Blade ink dots (2,3,4,5 psi).
- Fig. 31           Blade ink dots (5,6,7,8,10 psi).
- Fig. 32           Blade ink dots (twelve jets at 7 psi) .
- Fig. 33           Normalized velocity distribution along the blade surface with twelve wall  
jets installed ( $Re=232000$ ).
- Fig. 34           Endwall ink dots (with twelve wall jets installed).
- Fig. 35           Velocity Field and Total Pressure Losses - W/O JETS.
- Fig. 36           Velocity Field and Total Pressure Losses - W/ JETS.
- Fig. 37           Total Pressure Losses - w/ full fence.

## TABLE OF CONTENTS

|   |           |
|---|-----------|
| <b>ABSTRACT</b>                           | <b>1</b>  |
| <b>NOMENCLATURE</b>                       | <b>2</b>  |
| <b>LIST OF FIGURES</b>                    | <b>3</b>  |
| <b>1 INTRODUCTION</b>                     | <b>6</b>  |
| <b>2 EXPERIMENTAL APPARATUS</b>           | <b>13</b> |
| 2.1 WIND TUNNEL                           | 14        |
| 2.2 TURBULENCE GENERATOR                  | 15        |
| 2.3 TEST SECTION                          | 16        |
| 2.4 BLADE GEOMETRY                        | 17        |
| 2.5 LIQUID CRYSTALS AND RESISTANCE HEATER | 18        |
| 2.6 ENDWALLS                              | 19        |
| 2.7 FLAPS                                 | 19        |
| 2.8 FENCE                                 | 19        |
| 2.9 WALL JETS                             | 20        |
| <b>3 INSTRUMENTATION</b>                  | <b>21</b> |
| 3.1 A/D CONVERTER                         | 21        |
| 3.2 HOT-WIRE ANEMOMETER AND PROBE         | 21        |
| 3.3 PRESSURE TRANSDUCER                   | 22        |
| 3.4 PITOT TUBE                            | 23        |
| 3.5 KIEL PROBE                            | 23        |
| 3.6 LASER DOPPLER ANEMOMETRY              | 24        |
| <b>4 FLOW VISUALIZATION</b>               | <b>26</b> |
| 4.1 OIL AND BLACK POWDER TECHNIQUE        | 26        |
| 4.2 INK DOT FLOW VISUALIZATION            | 26        |
| 4.3 SINGLE TUFT PROBE                     | 27        |
| 4.4 VORTICITY DETECTOR PROBE              | 28        |

|          |  |           |
|----------|--|-----------|
| <b>5</b> | <b>QUALIFICATION OF THE TEST SECTION</b> | <b>29</b> |
| 5.1      | REYNOLDS NUMBER                          | 30        |
| 5.2      | PRESSURE DISTRIBUTION                    | 31        |
| 5.3      | BOUNDARY LAYER THICKNESS                 | 31        |
| 5.4      | SADDLE POINT                             | 32        |
| 5.5      | LOCATION OF HORSESHOE VORTEX             | 33        |
| 5.6      | BLADE INK DOTS                           | 34        |
| 5.7      | LIQUID CRYSTALS                          | 35        |
| 5.8      | SINGLE TUFT AND VORTICITY DETECTOR       | 36        |
| <b>6</b> | <b>ENDWALL FLOW MODIFICATION RESULTS</b> | <b>38</b> |
| 6.1      | WALL JETS NEAR THE SADDLE POINT          | 38        |
| 6.2      | OPTIMIZATION OF CHUNG'S FENCE            | 39        |
| 6.3      | ROW OF WALL JETS                         | 41        |
| 6.4      | VELOCITY FIELD                           | 45        |
| 6.6      | AERODYNAMIC PRESSURE LOSSES              | 46        |
| <b>7</b> | <b>CONCLUSIONS</b>                       | <b>48</b> |
|          | <b>REFERENCES</b>                        | <b>50</b> |
|          | <b>FIGURES</b>                           | <b>52</b> |

## 1 INTRODUCTION

---

Engineers are inevitably faced with technological limits and obstacles as they work toward achieving the highest possible efficiency of gas turbine engines. Currently a research program, the Integrated High Performance Turbine Engine Technology Initiative (IHPTET), whose members include engine companies such as Pratt & Whitney, General Electric, NASA, and the United States Military, are diligently working towards increasing the propulsion capability of gas turbine engines. The goal of this program is to double the thrust to weight ratio of aircraft engines. An increase in efficiency of the gas turbine engine will significantly increase the performance of our military aircrafts, ships, and industries. Technological advances made through research will ensure that the United States continues to be a leader in military gas turbine engines.

Gas turbine engines are vital components to our military forces. The gas turbine is a power generating device which supplies large amounts of power for a small physical size. Applications of gas turbines engines include jet engines, ship engines, helicopter engines, power generators and offshore power plants. Schematics of gas turbine engines are shown in Figures 1 and 2. Power is generated in an engine over three stages. In the first stage the pressure of atmospheric air is increased in a compressor. Energy is then added to the high pressure air by spraying fuel into the air, and burning the mixture in the combustion chamber. The combustion process creates a high temperature flow. This high-pressure, high-temperature gas then enters the turbine where it expands down to a lower pressure. The expansion process drives a shaft, thus producing power. Part of the power is used to drive the compressor. The rest of the power may be used to power a

generator or turn a propeller. In the case of a jet engine, instead of producing additional power in the turbine, the gas is further expanded and accelerated through a nozzle to provide thrust, which moves the aircraft forward.

Today's engineers are faced with the contradicting design goals for gas turbine engines of higher cycle efficiency and increased durability (Yeh and Gladden, 1989). In order to have higher cycle efficiency and produce increased power from the turbine, the turbine inlet temperature should be as high as possible. Over the past two decades improvements have been made in increasing turbine inlet temperatures to temperatures as high as 1981 K (Lakshminarayana, 1996). This temperature is limited by the durability of the turbine blades. High temperatures exceed the material limits of the blades, which experience tremendous thermal loads (forces due to high temperatures). The operating condition is in the range where thermal stresses rise and yield strengths fall. Even with the use of advanced composite materials which are capable of withstanding severe thermal loads, "hot spots" will occur along the blades due to the complex secondary flow between adjacent blades.

Figure 3 shows the blade and endwall configuration of a gas turbine engine. The endwalls are the surfaces of the hub and shroud, to which the blades are attached. Figure 4 is a schematic of two adjacent turbine blades and the terminology associated with them and the turbine passage. The greatest increase in turbine efficiency thus far has been due to improved cooling of these turbine blades (rotor blades and nozzle vanes) and the endwalls (Ito, 1978). One common cooling method is "film cooling" in which cool air is bled from the compressor and supplied to the inside of the blade. The bleed air seeps out

through small cooling holes machined in the blade and endwall surfaces, providing the blades with a protective film of cool air.

Effective film cooling of turbine blades is complicated by secondary flows, such as endwall vortices which interact with the turbine blades. The complex flow in the turbine passage is illustrated in Figure 5 (Chen and Goldstein, 1991). This figure shows a model of the vortical flows that develop along the passage between two adjacent turbine blades.

The turbine blade is shaped much like an airfoil. Because of the airfoil shape, the air flowing on the suction side of the blade (shown in Figure 5) has a farther distance to travel than the air flowing on the pressure side of the blade in the same amount of time. Therefore, the air flowing on the suction side of the blade must travel at a higher speed. This creates a low pressure area on the suction side of the blade, and a high pressure area on the pressure side of the blade. The pressure difference across the turbine passage causes a pressure gradient to form from the high pressure area to the low pressure area.

A vortex forms, due to the viscosity of air, at the junction of the turbine blade and endwall. The vortex hits the leading edge of the blade and splits. The suction side of the vortex wraps around the suction surface of the blade, while the pressure side of the vortex (named the horseshoe vortex), from the adjacent blade, migrates across the passage, due to the pressure gradient, and impinges upon the suction wall. The horseshoe vortex merges with the suction side vortex of the adjacent blade, and as these two vortices merge, they lift up off the endwall and increase in size. Figure 5 shows the horseshoe vortex impinging upon the suction side blade at point C and then climbing up the blade as it moves downstream. This vortex washes away the film cooling air on the surface of the

blade, thus reducing its cooling effectiveness and resulting in a triangular shaped hot spot, as documented by Langston et al. (1977).

Another characteristic of secondary flow, in the turbine passage, is the development of the saddle point near the leading edge of the pressure side blade, as shown in Figure 6 (Langston, 1977). Langston described the saddle point as the intersection of the attachment line and the separation line that divides the endwall flow into four distinct regions. The saddle point is a region from which the two dimensional endwall flow diverges. This can clearly be seen in Figure 6, illustrated by flow arrows. The concept of saddle point is discussed further in section 5.4 and illustrated through various flow visualization techniques.

Various methods have been developed to study and modify the secondary flow between two adjacent blades in an effort to increase turbine inlet temperatures while keeping the turbine blades below their thermal limits. These include techniques which attempt to divert the path of the horseshoe vortex. Several researchers such as Dossena et al. (1998), Duden et al. (1998), and Michelassi et al. (1998) are devoting their studies to turbine efficiency as well. They have focused on endwall contouring and 3D airfoil design in an attempt to reduce the secondary flow in the turbine passage.

In another study, Chung (1992) used a triangular shaped fence, inserted on the endwall between two adjacent blades. The fence was shaped into an equilateral triangle, and placed in the passageway as shown in Figure 7. This fence blocks and changes the path of the pressure side leg of the horseshoe vortex. The leading edge of the fence was located at the intersection of the leading edge pitch line and the center line between the

two adjacent blades. It extended downstream to 88% of the length of the chord. The fence acts like a ramp to lift the vortex up off the endwall to be washed away by the main flow. It was effective in preventing the vortex from growing to its full potential strength and diverting it away from the suction side blade. Since the influence of the secondary flow on the suction wall was reduced, film cooling would be more effective in that area. Additional aerodynamic losses (total pressure losses) due to secondary flow within the passageway are also reduced by the fence. Once lifted off the endwall the horseshoe vortex is no longer able to use the velocity gradient of the endwall boundary layer to produce additional circulation, therefore, the growth of the vortex is reduced. Flow visualization and data substantiating the effectiveness of Chung's fence will be discussed in further detail in section 6.2. Chung made no attempt to optimize the fence with respect to location and size. In practice, problems with this method arise due to a need to cool the fence itself (Chung, Simon and Buddhavarapu 1991).

The objective of the present study is to develop a method to reduce the harmful effects of secondary flow in a turbine passage without adversely affecting the aerodynamic performance of the turbine. As with the fence used by Chung (1992), an attempt was made to divert the path of the horseshoe vortex so that it would be washed away by the main freestream flow. Therefore, the vortex would never impinge upon the suction side blade. This should increase the effectiveness of film cooling on the suction surface and minimize the triangular hot region. In addition to protecting the suction side wall, it was hoped that weakening the vortex would decrease the aerodynamic losses in the passageway associated with the endwall secondary flow.

Two techniques were employed in order to achieve these objectives. First, wall jets were installed at a location downstream of the saddle point near the pressure side blade in an attempt to intercept the horseshoe vortex just downstream of its origin. Second, a row of wall jets were installed in a location similar to the fence studied by Chung (1992).

It was hypothesized that a row of jets might serve the same purpose in diverting the vortex as Chung's (1992) fence. The use of jets would circumvent the problem of having to manufacture and cool a fence. A fence similar to Chung's (1992) was constructed and modified, in length and orientation, to find the shortest length of fence that would still be effective in diverting the horseshoe vortex. Wall jets were then installed to take the place of the modified fence. The shorter the distance of the fence, the fewer the number of jets needed to cover that distance. The lower the number of jets, the lower the amount of air that is injected in the test section. Less injected air is desirable because, in a real turbine, cooling air reduces the temperature of the main mass flow thus reducing the power available from the turbine.

One study which considered the interaction between endwall blowing and a vortex was made by Ligrani and Mitchell (1994). They considered the effect of a vortex on film cooling. The air flow from the film cooling holes were relatively weak, so it did not affect the vortex dynamics. Other recent studies have considered the gap leakage between adjoining blade sections. One such example is provided by Chyu et al. (1998). It is suggested that leakage flow might be utilized to influence the vortex dynamics in a turbine

passage. In the present study the deliberate diversion of a vortex through a jet of air blowing from the endwall is considered.

## 2 EXPERIMENTAL APPARATUS

---

Modifying and gathering experimental data from an actual turbine would be an extremely expensive procedure. A more practical method is to study the effects of only some of the important variables of turbine passage flow. This can be done by modeling the turbine passage with a relatively simple facility, setting most of the important dimensionless variables, such as the Reynolds number, to match those of an actual turbine engine, and then modifying one of the variables to determine the effect it has on the flow and heat transfer.

Chung and Simon (1990) proved that a turbine cascade simulator can accurately model the passage flow of a turbine cascade. A turbine cascade is a series of several blades which model a stage of an actual turbine, as shown in Figure 8. A cascade simulator has a single passage, representing the flow between two adjacent blades in a cascade. Chung and Simon (1990) compared a cascade simulator to the seven-blade cascade study of Chen (1988). They used various flow visualization techniques such as oil and lampblack flow visualization, ink dot flow visualization, single tuft probe, tuft grids, and surface tuft sheets to insure that the cascade flow was replicated. Several of these techniques were used in the present study and are described below. The two-half-blade test section used by Chung and Simon displayed the main characteristics of the cascade flow, including the correct horseshoe vortex path, the saddle point location, the crossflow on the endwall, the rising of the passage vortex on the suction side blade, and the correct pressure distribution in the two-dimensional region away from the endwalls.

A large-scale, two-half-blade test section is built to simulate a turbine passage. Flow visualization and measurements are conducted to insure that the test section flow of the present study matches that of an actual turbine cascade. The Reynolds number and blade geometry of the present study's test section are matched to that of a CF6-50 General Electric gas turbine blade. The suction side wall is heated by a resistance panel heater. Cool inlet atmospheric air is blown over the turbine blades, creating a horseshoe vortex at the leading edge of each blade. The horseshoe vortex enhances the cooling of the suction side blade. The "cold spots" in this study coincide with "hot spots" on the actual turbine blades of an engine. Once the main characteristics of the flow were correct, two methods were tested in an attempt to divert the horseshoe vortex in order to decrease the aerodynamic losses in the passage, and improve film cooling effectiveness on the suction blade.

### *2.1 Wind Tunnel*

The wind tunnel used in this experimental study is a low-speed wind tunnel located in the Aeronautics Laboratory at the United States Naval Academy. This wind tunnel was designed and constructed at the Naval Academy by the Technical Support Division. It is a blower type configuration with velocities ranging from 0 to 18 m/s at the exit of the contraction. Air at room temperature is drawn into the wind tunnel by three 5-HP Dayton blowers (model 4C330). Each blower is powered by a 5-HP Dayton Industrial Motor 5HP (model 3N559A). The speed of each motor can be varied using a variable frequency controller (Mitsubishi General-Purpose Inverter, Model A024). The frequency of the AC

current, which powers the motors, is directly proportional to the motor speed and is altered by the controllers, stepping it down from the 60 Hz line frequency.

Following the blowers are the plenum, diffuser, two settling chambers, a screen pack, and nozzle as shown in Figure 9. The plenum is a 60 cm by 60 cm box with one open side and three 15 cm diameter holes on the opposite side connected to the blowers with flexible ducting. The flexible ducting isolates the rest of the facility from any blower vibrations. The plenum serves as a connection point for the blower before the flow enters the diffuser. The diffuser expands the air, decreasing the velocity, in order to make the flow more uniform. It also contains four screens which aid in producing flow uniformity. The settling chambers are open-ended boxes of dimensions 63.5 cm X 109 cm X 109 cm long. The first settling chamber contains honeycomb. The honeycomb acts to straighten the flow, removing any unwanted large scale flow structures. The screen pack consists of four fine (26 mesh) stainless steel screens. These screens cause a pressure drop, helping to make the flow more uniform, and reduce the turbulence level. The nozzle is a three-dimensional contraction which reduces the wind tunnel cross-sectional area by a factor of 9.8, thus increasing the velocity of the air. The acceleration in the nozzle also aids in improving flow uniformity and reducing the turbulence level. The nozzle exit area is 18 cm X 69 cm.

## 2.2 Turbulence Generator

To produce free-stream turbulence levels representative of a gas turbine environment, a turbulence grid was used. The turbulence generator, shown in Figure 10

(Stoddard, 1998), is an open ended, rectangular plexiglass box which attaches to the nozzle of the wind tunnel. At the upstream end, the box holds a two dimensional bar grid consisting of one vertical 1.5-inch diameter PVC pipe, and six horizontal 1.25-inch diameter PVC pipes, evenly spaced across the nozzle outlet. The grid is followed by a one meter long rectangular settling chamber which allows the flow to become uniform before entering the test section. This turbulence generator creates 10.7% free-stream turbulence intensity, while maintaining uniformity in the mean flow to within  $\pm 2.8\%$ . The turbulence level is uniform to within 3.6%. This turbulence intensity is representative of gas turbine environments. Further details are available in Stoddard (1998).

### *2.3 Test Section*

The test section is attached downstream of the turbulence generator, as shown in Figure 11. It contains two turbine half-blades modeling the turbine passage, a top and bottom endwall, and two flaps to guide the flow into the test section, providing the proper leading edge flow on the blades to match a multi-blade cascade. The geometry of the test section and the test conditions are summarized and compared with Chung's (1992) test section geometry and conditions in Table 1.

|                              | Chung (1992) | Present study |
|------------------------------|--------------|---------------|
| Chord (mm)                   | 231          | 328           |
| Pitch (mm)                   | 178          | 252           |
| Span (mm)                    | 610          | 665           |
| Aspect Ratio (H/C)           | 2.64         | 2.02          |
| Solidity (C/P)               | 1.30         | 1.30          |
| Inlet Angle (deg)            | 44.3         | 46            |
| Outlet Angle (deg)           | 62.7         | 62            |
| TI (%)                       | ~10          | ~9            |
| $\delta_2/C$ at leading edge | 0.011        | 0.010         |

**Table 1** Test section geometry and test conditions

#### 2.4 *Blade Geometry*

The test section blade shape is the General Electric CF6-50 profile, scaled up to have a chord length of 328 mm, as shown in Figure 12. This is the same blade shape used in the multi-blade cascade of Chen (1988) and in the two-half blade cascade simulator used by Chung (1992). The leading and trailing edges of the pressure blade are machined out of high density foam and connected with transparent plexiglass to match the coordinates of the CF6-50 shape. Plexiglass was used to provide optical access to the test section. The suction side blade is machined out of foam to match the coordinates of the CF6-50 shape.

Static pressure taps were drilled in to the suction and pressure side blades of the test section at height of 356 mm above the endwall. The pressure taps are located away from the endwalls in a region where the flow is two-dimensional. The curvilinear distances of the static pressure taps from the stagnation line on the leading edge non-dimensionalized by chord length are presented in Table 2. Eleven pressure taps are located on each side of the blade, with an inner diameter of 0.3 mm. Tygon tubing

connects each pressure tap to a Scani valve with multiple ports. The outlet of the Scani valve is connected to a pressure transducer. The Scani valve cycles through each port to yield pressure data at the various static taps.

| Pressure Taps |              |
|---------------|--------------|
| Pressure Side | Suction Side |
| Sp/C          | Ss/C         |
| 0.193         | 0.27         |
| 0.257         | 0.337        |
| 0.0323        | 0.402        |
| 0.391         | 0.467        |
| 0.463         | 0.534        |
| 0.54          | 0.606        |
| 0.624         | 0.686        |
| 0.722         | 0.0777       |
| 0.785         | 0.884        |
| 0.829         | 0.995        |
| 0.913         | 1.113        |

**Table 2** Position of pressure taps on blades

### 2.5 Liquid Crystals and Resistance Heater

A surface resistance heater and liquid crystals are mounted on the suction side blade. The resistance heater, a thin sheet of coiled wires, wraps around the suction side blade from the endwall to a height of 255 mm. Electric current, controlled by 120 V AC variable auto-transformer, is passed through the resistance wires causing them to heat. This provides a uniform heat flux boundary condition. A sheet of cholesteric liquid crystals was applied over the heater. The molecular orientation of the cholesteric liquid crystals changes with temperature, causing a change in the liquid crystal color.

## 2.6 Endwalls

The endwalls serve as the top and bottom of the test section. They are constructed of 0.25 inch thick clear plexiglass. Both the top and bottom endwall have sharp leading edges which extend to the edge of the turbulence generator settling section. These edges serve to remove the boundary layer developed in the nozzle of the wind tunnel and the turbulence generator.

## 2.7 Flaps

Two transparent plexiglass flaps extend from the sides of the settling section to direct the flow into the turbine blade test section. A top view of this test section which illustrates the two half-blades and the two flaps is shown in Figure 11. The flaps curve out past the leading edge of the turbine blades. The gaps between the turbine blades and the plexiglass flaps, labeled a and b in Figure 11, are adjustable. These gaps allow air to escape the test section and exit to the atmosphere. By controlling the size of the gaps, the flow around the leading edges of the blades could be controlled. This affects the flow conditions, particularly the development of secondary flows, in the test section. The flaps were necessary because in an actual turbine some of the air would flow through the present blade passage as well as into the neighboring blade passages.

## 2.8 Fence

For the secondary flow modification study, fences were constructed of clay, to model the fence used by Chung (1992). The fence is placed in the same location as

Chung's, shown in Figure 7. It is constructed out of a clay triangular base, height 0.75 cm, and an index card. The total height of the fence is 2 cm (scaled up from the height of Chung's fence in proportion to the present study's test section). The length of the fence is 88% of the chord or 288 mm.

### 2.9 *Wall jets*

For the secondary flow modification study, various configurations of wall jets were used in an attempt to redirect the horseshoe vortex. All wall jets used in this study were of the same type, but used in varying configurations. Holes were drilled and tapped into the bottom endwall and fittings with inside diameter 6 mm were screwed into the holes. All jets are 8 mm apart. Shop air was used to supply air for the wall jets. The air was blown into a 2 gallon Nalgene bottle, the pressure inside the bottle was controlled with a pressure regulator. The bottle contained 12 taps with 3/16 inch imperial tubing leading from the taps to the wall jet fittings. In some cases clamps were used to restrict the flow in the imperial tubing in order to maintain a uniform velocity through all of the wall jets. Hot wire anemometry was used to measure the jet exit velocity.

### **3 INSTRUMENTATION**

---

#### *3.1 A/D Converter*

An A/D 488/8SA analog-digital converter, manufactured by IO Tech, converted voltage from various instruments, such as the hot-wire anemometer or pressure transducer, to a digital signal. The A/D converter is connected to a personal computer using an IEEE interface bus, and has 16 bit accuracy.

#### *3.2 Hot-wire Anemometer and Probe*

A single sensor, boundary layer type hot-wire probe (TSI model 1218AE-T1.5) was used in the present study with a hot wire anemometer (TSI IFA 100 System Intelligent Flow Analyzer). The hot-wire was used to measure the streamwise component of the test section inlet and outlet velocities, and the velocities of the wall jets. The hot-wire sensor is a thin (4  $\mu\text{m}$  diameter) wire which is used as a resistance element. It is heated and controlled at a constant temperature by the anemometer using a Wheatstone bridge. The amount of electrical energy necessary to maintain the constant temperature of the hot-wire is a measure of the cooling effect of the fluid flowing past the heated wire. The hot-wire probe is connected to the anemometer with a coaxial cable. The cooling effect of the fluid passing over the heated wire is both a function of mass flow and temperature difference. The relationship between the bridge voltage and flow velocity is given by

$$U = \left[ A + B * E^2 \frac{(t_s - t_c)}{(t_s - t)} \right]^{1/0.435} \quad (1)$$

which is a modified form of King's law (Volino and Simon, 1995). The variable U is the velocity, E is the anemometer bridge voltage,  $t_s$  is the hot-wire temperature (held at a constant 250° C),  $t_c$  is the calibration temperature of the hot-wire (25° C), and t is the air temperature during the experiment. The hot-wire was calibrated by placing it in a jet of known and adjustable velocity. A best fit of the data was performed to determine the constants A and B in Equation (1).

### 3.3 Pressure Transducer

A Valdyne pressure transducer with carrier demodulator was used to conduct pressure measurements. The transducer is constructed of a thin diaphragm which is deflected by a pressure difference. The diaphragm used in the present study had a range of 0 - 3.5 inches H<sub>2</sub>O. The carrier demodulator outputs a voltage which is proportional to the pressure difference across the diaphragm. A pitot tube was placed in the wind tunnel and connected to both the pressure transducer and the micromanometer. The output voltage of the transducer and pressure determined from the micromanometer was measured over a range of velocities from 2 m/s to 12 m/s in 2 m/s increments. The output voltage was plotted versus the pressure at each measurement and the slope of the best linear fit was calculated. This slope was used to calculate the pressure, given the pressure transducer output voltage.

### 3.4 *Pitot tube*

A pitot tube with a total pressure tap and a static tap was used to measure the total pressure in the wind tunnel. The pitot tube was also used to measure the inlet and exit velocities of the test section by applying Bernoulli's equation:

$$U_1 = \sqrt{\frac{2}{\rho}(P_t - P_s)} \quad (2)$$

where  $P_t$  is the total pressure and  $P_s$  is the static pressure.

### 3.5 *Kiel probe*

The Kiel probe is a total pressure probe, which is insensitive to angle. The insensitivity to angle was an important characteristic of the probe in this study because the exact direction of the flow was not known due to the strong secondary flow in the turbine passage. The Kiel probe was used to traverse a plane 28 mm upstream of the trailing edge of the suction side blade, as shown by Plane A in Figure 11. The plane was perpendicular to the blade surface and the endwall, and extended from the blade-endwall junction to 70 mm away from the suction surface, and 170 mm above the endwall. These data were used to determine the total pressure coefficient at each point measured in the plane. The total pressure coefficient was then used to document the total pressure loss distribution in the passageway near the trailing edge of the suction side blade. The total pressure coefficient,  $C_{p_t}$ , is defined as the difference between the local total pressure and

the total pressure of the flow upstream of the passageway near the leading edge pitch line; it is expressed as

$$Cp_t = \frac{P_t - P_{tr}}{0.5\rho U_1^2} \quad (3)$$

### 3.6 Laser Doppler Anemometry

Laser Doppler Anemometry (LDA) is a method designed to measure the flow velocity by measuring the Doppler shift of light scattered from small particles. As explained by Flack (1998), the LDA system used in the present study (Dantec Flowlite) uses a helium neon laser with wave length of 633 nm (red light), Gaussian beam diameter 1.68 mm and a crossing angle of 5 degrees. A fiber optic probe, containing the laser beams is mounted on a Dantec three axis traverse that moves the probe with precision in three degrees of freedom. Two equal intensity light beams are emitted from the laser and cross in the test section. The location of the beam crossing is controlled by a lens. When the two beams intersect an interference pattern is formed as a set of planar fringes. The fringes are parallel to the bisector to the two beams and perpendicular to the plane containing the beams. Particles that flow through the crossed laser beams scatter light which is collected by the LDA system and focused onto a detector. The detector uses a photo multiplier system to convert the total flux of light energy into a voltage. This voltage is input to a signal processor which determines the Doppler frequency in the photo detector output. The Doppler frequencies are converted to velocities (U) using the following equation:

$$U = f\delta \quad (4)$$

where  $\delta$  is the distance between interference fringes and  $f$  is the frequency of the Doppler shift.

Particles in the flow are necessary to scatter the light needed for the operation of the LDA. Two methods of flow seeding were used in this study. A Roscoe 1600 theatrical fog machine was connected to a 1.5 inch hole in the bottom of the wind tunnel in the second settling chamber. The fog machine uses specially designed fluid to create a fog which was added to the air flow.

Problems arose with the use of the fog machine as a particle supplier for the laser Doppler anemometry. The machine tended to coat everything with an oily film and to fill the room with fog. The high operating temperature of the machine caused the PVC piping, used to supply the fog to the wind tunnel, to melt. This limited the amount of continuous time the fog machine could be running.

A sonic nozzle water sprayer was used instead of the Roscoe 1600 fog machine for some velocity measurements. The water sprayer used compressed shop air to supply a jet pump with water and produce a fine spray of water. The water droplets provided a cleaner method of seeding the flow for the LDA than the fog machine.

## 4 FLOW VISUALIZATION

---

Various flow visualization techniques were employed to observe the characteristic of the three-dimensional flow in the test section passage. Flow visualization was used to show the shear stresses on the endwalls and the turbine blades, as well as the location of the horseshoe vortex and the saddle point area. These techniques are useful in validating the present test section as a facility for comparison to cascade flow studies.

### 4.1 *Oil and Black powder Technique*

A mixture of Starret M1 Lite Lube oil and copier toner was applied to the endwall to observe the direction of the endwall shear stresses. With this technique a piece of contact paper was taped to the endwall and covered the entire region between the turbine blades. A mixture of oil and copier toner, in a 15:3 ratio, was painted in a thin uniform layer over the contact paper. Upon exposure to the flow, the mixture moves in the direction of the endwall shear stresses so that black lines made by the copier toner indicate the direction of the flow. Areas where the toner is washed away completely indicate areas of high endwall shear stresses.

### 4.2 *Ink Dot Flow Visualization*

Ink dot flow visualization is a technique introduced by Langston and Boyle (1982). This technique provides a permanent record of the endwall shear stresses as shown by ink traces. A grid pattern of dots, with a spacing of 12 mm X 12 mm, was placed on a section of contact paper with a black Sharpie® permanent marker. The contact paper was then

taped to the endwall in the passage. A Preval® spray gun is used to spray a uniform thin layer of 99.5% isopropyl alcohol over the ink dots. In their studies, Langston and Boyle originally used oil of wintergreen as a solvent instead of isopropyl alcohol. Qiu and Simon (1998) used isopropyl alcohol in their ink dot technique and concluded that it would suffice for the flow visualization. The alcohol dissolves the ink dots and upon exposure to flow, the ink moves in the direction of the shear stress on the endwall. The alcohol evaporates and the ink traces dry, leaving a permanent record of the endwall shear stresses. About 45 seconds are required per run.

The ink dot flow visualization technique was used on the suction side blade as well as the endwall. A piece of contact paper 22.5 mm long and 10 mm high was adhered to the suction side blade, 3.8 mm upstream of the trailing edge of the suction blade and flush with the endwall. This technique was useful because it shows where the horseshoe vortex impinges upon the suction side blade.

Even in complicated flow regions, such as the saddle point area, the origin of the ink dot trace can be seen. Therefore, it is clear which direction the trace was traveling in. Another advantage of this technique is that even in areas of low velocity the direction of the local shear stress can be seen.

#### 4.3 *Single Tuft Probe*

The single tuft probe technique is used to show the flow pattern in the turbine passage and to locate the general position of the horseshoe vortex. A schematic of the single tuft probe is shown in Figure 13. A single piece of yarn ranging in length between

12 mm and 380 mm is tied around a steel loop of 4.75 mm diameter. The loop is connected to the end of a wand. This system allows for the tuft to rotate around the loop, providing freedom for the tuft to move in all directions. The direction of the yarn indicates the direction of the flow at the tip on the wand. When placed near the endwall a short piece of yarn shows the direction of shear stress on the endwall. When a long piece of yarn is placed in the passageway the location of the horseshoe vortex can be found, as indicated by the violent twirling motion of the yarn when it is inside the horseshoe vortex.

#### 4.4 Vorticity Detector Probe

The vorticity detector is used to locate the horseshoe vortex. The vorticity detector is a small pinwheel as shown in the schematic in Figure 14. Four thin cardboard pieces 1.5 mm by 1.5 mm were connected to a hollow straw of diameter 3 mm and length 2 cm with clear adhesive tape. The tube was slid over the 2 cm length of an L shaped steel wire of diameter 1 mm and handle length 13 cm. The vorticity detector probe is placed in the test section with its axis (shown in Figure 14) orientated upstream in the direction of the flow. The location of the horseshoe vortex can be located in this manner, as indicated by the twirling motion of the probe.

## **5 QUALIFICATION OF THE TEST SECTION**

---

The test section was qualified by comparison to the cascade simulator used by Chung (1992) to show that it is capable of reproducing the main features of the CF6-50 turbine passage flow. The pressure distribution at the center span of the blades was compared with predicted data from General Electric (GE) and data from Chung (1992) in a turbine cascade simulator of the same blade geometry and similar flow conditions. Flow visualization and boundary layer measurements were taken and compared to Chung's study to qualify the test section. The results from the pressure distribution, boundary layer measurement, and flow visualization are discussed below.

The main characteristic of the flow in the passageway were matched to those of Chung's study. Three of the main parameters were Reynolds number, boundary layer thickness and the location of the saddle point. These three parameters are not independent of each other, therefore the adjustment of one may affect the others. The setting and measurement of these three parameters were done by trial and error, and guided by an understanding of the process. The following procedure was used as criteria to compare the present study to that used by Chung (1992):

1. Set the speed of the wind tunnel to match the value of the Reynolds number in Chung (1992).
2. Slightly adjust the blade orientation in order to match the expected pressure distribution for the CF6-50 blade.

3. Trip the endwall boundary layer at the inlet to the test section to produce the desired boundary layer thickness entering the passage to match Chung's (1992) results.
4. Position the flaps to change the gap between them and the turbine blade in order to adjust the location of the saddle point.
5. Locate the position of the horseshoe vortex.

### 5.1 *Reynolds Number*

The Reynolds number (Re) is a dimensionless parameter used to describe the incoming flow given by

$$\text{Re}_c = \frac{U_1 C}{\nu} \quad (5)$$

where  $U_1$  is the inlet velocity,  $C$  is the blade chord and  $\nu$  is the kinematic viscosity of the air. Flow similarity between various experiments can be obtained through geometric similarity and Reynolds number. The Reynolds number used in this study was approximately 232000, which matched the experiments of Chung (1992).

The wind tunnel was turned on with all three motors operating at the same frequency. The tunnel velocity was measured using a pitot-static tube to determine the Reynolds number at which the wind tunnel was operating. The frequency of the motors were then changed to adjust the speed of the air until the Reynolds number equaled 232000. All three motors always operated at the same frequency.

### 5.2 *Pressure Distribution*

The variation of free-stream velocity  $U_1/U_2$  as a function of pressure tap position, over both the pressure and suction side blades is presented in Figure 15. The latter figure shows the pressure distributions for the present study's test section in comparison with Chung's (1992) cascade simulator pressure distribution, the pressure distribution used by Ito (1978) in his study of a turbine cascade, and with that of the predicted values of velocity ratio supplied by General Electric (GE). The present case compares well with the predicted values supplied by General Electric. On the suction side, the velocity rises rapidly up to  $1.13U_2$  at  $S_s/C=0.276$ , this shows that there is a rapid acceleration on the leading edge of the suction blade. The velocity is almost uniform along the first half of the blade, with a slight increase at  $S_s/C=0.686$  up to  $1.23U_2$  and then a gradual decrease along the rest of the blade to  $1.1U_2$  at  $S_s/C=1.113$ . On the pressure side, the velocity rises rapidly up to  $0.36U_2$  at  $S_p/C=0.193$ . This shows an acceleration on the leading edge similar to that on the suction side but of a much smaller magnitude. This is followed by a region of almost constant velocity and then a strong increase in acceleration around the pressure side of the blade reaching  $0.81U_2$  at  $S_p/C=0.913$ .

### 5.3 *Boundary Layer Thickness*

Laser Doppler Anemometry was used to measure the inlet boundary layer thickness at a location 25.5 cm upstream of the leading edge of the pressure side blade, near the center of the passage. From this data,  $\delta_2/C$ , momentum thickness over chord, was calculated by extrapolating the boundary layer growth from this position to the

leading edge of the pressure side blade assuming a flat plate, zero pressure gradient, turbulent boundary layer. The inlet boundary layer was made turbulent using a 1/8 inch Tygon tube to trip the endwall boundary layer at the entrance of the test section, just after the settling section. The size of the trip was selected to match the value of  $\delta_2/C$  reported by Chung (1992).

#### 5.4 *Saddle Point*

The ink dot flow visualization technique was employed to determine the location of the saddle point in the test section. The saddle point is the location on the endwall where the flow from opposite directions merges and is directed outward at right angles from the endwall. The entire flow field near the endwall is split into four distinct regions by the attachment line and the separation line, as discussed by Langston (1977), and shown in Figure 6. The intersection of the lines indicates a singularity in the endwall shear stress.

Figure 16 shows the ink dot flow visualization done by Chung and Simon (1993). The position of the saddle point is indicated by the X. This picture is used as a model for comparison to the ink dot flow visualization of the test section in the current study.

Figure 17 presents the ink dot flow visualization for this study, with the location of the saddle point marked by an X. One can clearly see that the direction of the endwall shear stresses in each region is matched to those of Chung and Simon (1990). The location of the saddle point is along the pitch line near the leading edge of the pressure side blade, as shown in Figure 17. Chung (1992) discovered that the location of the saddle point was

insensitive to the position of the flaps as long as the gap was in the range of 1.2 cm to 3.0 cm. With the flaps of the present study within this range, the location of the saddle point was satisfactory. The values 1.5 cm and 1.25 cm were chosen out of convenience for the size of the gaps at locations a and b respectively, as illustrated in Figure 11. These values are fixed throughout the entire study.

The location of the saddle point is also illustrated by the oil and black powder technique. Photographs were taken from the top of the test section looking down onto the passageway to show the movement of the oil and black powder. The saddle point, shown in Figure 18, appears at the same location as shown in the ink dots and black powder visualization of Chung's cascade. The separation and reattachment can be seen as lines of concentrated black powder. Where they cross, an X is formed, which corresponds to the location of the saddle point. The region is dark because it is an area of low shear stress and the powder accumulates there without being swept in any direction. The single tuft probe also shows the location of the saddle point by pointing in the direction of the shear stresses in each of the four regions surrounding the saddle point.

### 5.5 Location of the horseshoe vortex

Further analysis of the ink dot pattern shows the shear stresses on the endwall, the location of the stagnation point, and the horseshoe vortex in the flow. Figures 19 and 20 are ink dot patterns for the endwall of Chung's study and the present study respectively. The stagnation point is the location where the velocity is zero on the blade. Here the flow splits and moves on opposite sides of the blade. The location of the stagnation point is

indicated in each of these figures. The endwall shear stresses in the present study match well with the shear stresses in Chung (1992), as shown by the ink dot flow visualization (Figure 19). The cross flow due to the pressure gradient from the pressure side blade to the suction side blade is clearly indicated. The location of the horseshoe vortex can be seen downstream of the saddle point, near the leading edge of the pressure side blade, and continuing across the passage way toward the suction side blade. The ink dot traces show the clockwise sense of rotation of the horseshoe vortex ( view looking upstream). This is the sense of rotation of the vorticity of the inlet boundary layer as discussed by Langston (1977).

Analysis of the oil and black powder visualization of Chung's (1992) and the present study, shown in Figure 21, illustrates the same flow characteristics. The migration of the horseshoe vortex from the pressure side blade to the suction side blade is illustrated by the white line through the passage, where the shear stresses are maximum. The vortex eventually impinges upon the suction side blade. The streak lines from the pressure side blade to the suction side blade are indicative of the crossflow caused by the pressure gradient in this region.

### 5.6 *Blade Ink Dots*

The ink dot flow visualization done on the suction side blade, as described in section 4.2, provides a clear pattern of shear stresses on the blade, as shown in Figure 22. In some areas the ink was smeared due to the accumulation of alcohol from upstream and should be disregarded. The clockwise rotation of the vortex moves the ink traces in an

upward motion. Although each ink trace shows the direction of shear stress, not the magnitude, a general idea of the magnitude of the shear stresses can be deduced by the angle of inclination of the ink trace. The location of the horseshoe vortex can be seen as quite strong in the area of upward ink traces. The ink traces above the vortex are straight lines in the direction of the main flow indicating that the horseshoe vortex has no effect in this area. The slight downward inclination of some traces is due to the fact that the ink dissolves in the alcohol and starts to run down, as a result of gravity, before the wind tunnel reaches its full velocity. Chung arrived at a similar conclusion when looking at the effect of the horseshoe vortex on the pressure side blade through ink dot flow visualization.

### 5.7 *Liquid Crystals*

Liquid crystals give a good indication of the heat transfer on the suction side blade. It can clearly be seen by the drastic change in color that the area nearest the junction of the suction side blade and the endwall is cooler than the rest of the blade. This is caused by the suction side of the horseshoe vortex wrapping around the suction surface of the suction blade. Further downstream on the blade one can see that the cooled area increases in size and moves up the blade. This cooling is due to the pressure side of the horseshoe vortex from the neighboring blade impinging upon the suction side blade. This vortex merges with the suction side vortex near the endwall and moves up the blade. This vortex creates a hot spot on an actual turbine blade, corresponding to the cool spot indicated by the liquid crystals on this test section.

Although the liquid crystals are a good indication of the presence of the vortex on the suction wall, the technique was not sensitive enough to indicate changes in cooling due to vortex modifications.

### 5.8 Single Tuft Probe and Vorticity Detector Probe

With the use of a single tuft probe it is easy to find the general location of the horseshoe vortex. A single tuft probe placed between the two blades and far from the endwall, points in the direction of the suction side blade. This occurs due to the pressure gradient in that direction. When the tuft is located near the endwall, the location of the horseshoe vortex is indicated by the violent twirling motion of the tuft. A long tuft reaching from the inlet of the passageway to the trailing end of the suction side blade shows how the vortex increases in size and moves up the blade. This is evident by the large twirling motion of the tuft in the trailing edge area. The tuft also hits the suction side blade in an area corresponding to the cooled areas as shown by the liquid crystals. If the tuft is lifted off the endwall, the twirling motion stops and the tuft points in the steady direction of the pressure gradient. The tuft no longer hits the suction side blade. It is pushed toward that blade due to the pressure gradient but never impinges upon the blade. This phenomenon supports the idea that if the horseshoe vortex is pushed up off the endwall it will be washed away by the main stream flow, therefore never impinging upon the suction side blade.

The vorticity detector probe is used in a similar manner to that of the single tuft probe. When oriented so that the axis of the probe is pointed upstream in the direction of the flow (as discussed in section 4.4), the streamwise vorticity causes the probe to spin. When the probe is pulled up off the endwall, or away from the effects of the horseshoe vortex, the spinning motion stops. The effects of the horseshoe vortex can be seen by the spinning of the probe beginning at the leading edge of the pressure side blade. The horseshoe vortex can be followed by traversing the probe across the passage, against the suction side blade, and out of the test section.

## 6                      ENDWALL FLOW MODIFICATION RESULTS

Three different methods were used in attempts to modify the test section endwall flow. The horseshoe vortex, that forms at the junction of the leading edge of the pressure blade and the endwall, is one aspect of secondary flow in a gas turbine that limits the effectiveness of film cooling. Each of the methods in the present study was directed at changing the path of the horseshoe vortex. The vortex impinges upon the suction side blade, increasing in size and climbing the blade as it proceeds downstream. Figure 23 illustrates the path of the horseshoe vortex (dotted-line vortex) across the passage, and impinging upon the suction side blade (Chung, 1992). Chung proved that changing the path of the horseshoe vortex is effective in reducing secondary flows and in decreasing the aerodynamic losses within the passageway.

### *6.1 Wall jets near the saddle point*

Five wall jets were installed near the saddle point in the locations illustrated in Figure 24. This method attempted to redirect the horseshoe vortex near its point of origin. The wall jets were located just downstream of the saddle point at the junction of the leading edge of the pressure side blade. This is where the horseshoe vortex forms according to the ink dot and black powder visualization of the endwall, as discussed in section 5 (Figures 20 and 21).

Analysis of the secondary flow with the single tuft probe revealed that the horseshoe vortex still impinges upon the suction blade, as in the case without any jets. When the tuft was placed near the endwall, in the passageway, it moved in a violent

twirling motion. This motion is indicative of the location of the horseshoe vortex. When the tuft was placed near the endwall and suction side blade, the horseshoe vortex could still be detected by the probe.

The vorticity detector showed that the horseshoe vortex appeared to travel around the jets towards the pressure side blade, when jet #3 was not operating, and then migrate across the passage. When jet #3 was operating the vortex appeared to travel through the jets and migrate across the passageway, not affected by the jets. Ink dot flow visualization on the suction side blade with the jets near the saddle point, shown in Figure 25, was compared with the case without wall jets (Figure 22). There is a slight change in the inclination of the ink traces between these two figures, but it is of no significant difference. In each case the wall jets proved to be ineffective in reducing the impinging effect of the horseshoe vortex upon the suction side blade.

## 6.2 Modification of Chung's Fence

A fence, similar to that used by Chung (1992), was modified to minimize its length. This was done in preparation for the use of a row of wall jets described below. The wall jets were to be installed in place of the fence at the same location as the fence. By minimizing the length of the fence, the number of wall jets could be reduced, thereby reducing the amount of air required.

A clay fence, used to model the fence of Chung (1992), was positioned in the test section as discussed in section 2.8, and shown in Figure 7. The criterion used to evaluate the effectiveness of the clay fence is ink dot flow visualization on the suction side blade.

Figure 25 shows blade ink dots with the full fence in place. With the presence of the fence, the ink traces clearly show that the effects of the horseshoe vortex on the suction side blade have been reduced. The mild inclination of the ink traces near the endwall is due to the secondary crossflow caused by the pressure-suction gradient, and is not associated with the horseshoe vortex. These results are consistent with similar results obtained by Chung (1992). Chung concluded that with the fence, the horseshoe vortex could not reach the suction side blade. Instead, it is lifted by the fence and washed away by the mainstream flow.

Evaluation of the flow by the single tuft probe and the vorticity detector led to the same conclusion. The single tuft probe was pushed in the direction of the cross flow, but the horseshoe vortex was not detected on the side of the fence near the suction blade. At a similar location, when the vorticity detector does not twirl, this indicates that there is no vortex in that region.

Once it was concluded that the fence in this study redirected the horseshoe vortex, just as Chung's (1992) fence did, attempts were made to optimize the fence. The fence was split into 8 equal sections, each 36 mm long. Ink dot flow visualization was done on the suction side blade to see the effect of the removal of each section of the fence. The results of this inspection are shown in Figures 25 and 26.

With the removal of the upstream two sections of the fence and the downstream two sections of the fence, the remaining sections still proved to be effective in diverting the horseshoe vortex. This result was demonstrated by inspection of Figures 25 and 26. The orientation of the shortened fence was then modified to find the most effective one in

reducing the horseshoe vortex on the suction side blade, as shown by the ink traces. Different orientations showed different effects (with blade ink dots) of the horseshoe vortex on the suction side blade. The results of the initial and final orientations are shown in Figure 27.

A fence configuration, 44% of chord length, was sufficient in redirecting the horseshoe vortex. A schematic depicting the location and orientation of the modified fence is shown in Figure 28. Notice the leading edge of the fence is slightly turned toward the suction side blade. In this position the horseshoe vortex is intercepted and forced to follow a path along the fence.

Oil and black powder visualization were conducted with the modified fence in place. The separation saddle point could be seen at the same location as in the case without any flow modifications, as shown in Figure 21. The horseshoe vortex develops just down stream of the saddle point, near the leading edge of the pressure blade, and proceeds to migrate across the passageway. The fence intercepts the vortex and forces it to travel the length of the fence and exit the passage at the trailing edge pitch line.

### 6.3 Row of Wall Jets

Twelve wall jets (as described in section 2.9) were installed in place of the modified fence. It was assumed that the wall jets would perform the same function as the fence by lifting the horseshoe vortex off the endwall and diverting it from the suction side blade. The configuration of the twelve wall jets is shown in Figure 29.

The blade ink dot technique was the first one used to evaluate the effectiveness of the wall jets. The pressure in the Nalgene bottle was varied from 2 psig to 10 psig in increments of 1 psig. The results of the blade ink dots as a function of pressure is shown in Figures 30 and 31. It was concluded, by inspection of the blade ink dots, that a pressure of 7 psig supplied enough air to successfully divert the horseshoe vortex. A blown up image of the ink traces on the suction side blade, with the jets at 7 psig, is shown in Figure 32. Hot-wire anemometry is used to measure the velocity of each of the twelve wall jets at 7 psig. The results of these measurements are given in Table 3.

| Jet # | Velocity (m/s) |
|-------|----------------|
| 1     | 21.15          |
| 2     | 25.86          |
| 3     | 22.75          |
| 4     | 25.92          |
| 5     | 25.83          |
| 6     | 21.27          |
| 7     | 22.14          |
| 8     | 25.04          |
| 9     | 24.86          |
| 10    | 23.42          |
| 11    | 23.72          |
| 12    | 25.10          |

note: jets are numbered from leading edge to trailing edge

(orientation shown in Figure 29)

**Table 3** Velocities of the row of twelve jets operating at 7 psig

The average jet velocity associated with the 7 psig pressure was 23.92 m/s. The exit velocity to the test section,  $U_2 = 13.75$  m/s. The blowing ratio  $(\rho U)_{jet}/(\rho U)_2 = 1.7$ . The momentum ratio  $(\rho U^2)_{jet}/(\rho U^2)_2 = 2.9$ . Typical blowing ratios for film cooling are well below 1, but this is due to the film cooling being more effective at lower blowing ratios.

In practice, a velocity ratio ( $U_{jet}/U_2$ ) approaching 1 should be possible even in the first stage. The ratio of the turbine inlet temperature to the compressor exit temperature ( $T_2/T_{jet}$ ) is approximately 3 (Lakshminarayana, 1996). Because pressure is approximately constant during the combustion process, the density ratio ( $\rho_{jet}/\rho_2$ ) may also approach 3. Therefore, a blowing ratio of 3 should be possible. A momentum ratio of 3 should also be possible. The blowing ratio of the present study should be achievable in an actual engine. The momentum ratio in the present study is somewhat high; however, it is of the same order as that achieved in an engine. The experiments in the present study were done with a density ratio ( $\rho_{jet}/\rho_2$ ) of 1.0, while in an actual turbine engine the ratio would be much higher. To determine more precisely the blowing and momentum ratios needed for the jets for comparison to engine condition, further experiments should be done with jets at a high density.

Lakshminarayana (1996) states that the typical cooling requirement in the first stage nozzle is 6.4% of the core engine inlet flow. Therefore the mass flow of the jets in the present study is within reasonable bounds for practical engine operation. The mass flow from all 12 jet is 3.9% of the mass flow through a typical turbine passage, assuming an aspect ratio of 1.0 and blowing from the top and bottom endwalls.

The variation of the normalized free-stream velocity  $U_L/U_2$  as a function of pressure tap position, over both surfaces of the blade is shown in Figure 33. The normalized velocity distribution as predicted by General Electric is compared with the distribution arrived at by Chung (1992), and the distribution in the present study for the case with no jets installed and for the case with twelve wall jets installed. Comparison of

the pressure distribution with twelve jets installed and the distribution with no jets, indicates that the wall jets have no effect on the pressure distribution within the turbine passage.

The ink dot technique was applied over the entire passageway endwall, with wall jets. The result of the ink traces are shown in Figure 34. This figure shows that the main characteristics of the flow, excluding the horseshoe vortex path, are similar to the case without the wall jets. The saddle point is located in the same position. The endwall crossflow due to the pressure gradient from the pressure side blade to the suction side blade is clearly indicated. The horseshoe vortex is observed downstream of the saddle point, near the leading edge of the pressure side blade. The vortex begins to migrate across the passageway, toward the suction side blade, but is intercepted by the wall jets. The vortex is pushed along the length of the wall jet row and out of the test section.

The oil and black powder technique was applied to the test section with the twelve wall jets operating at 7 psig. Once again when compared with the case without any flow modifications, Figure 21, there are no significant changes in the flow characteristics, besides the diversion of the horseshoe vortex. The location of the saddle point and the endwall cross flow are clearly evident. The path of the horseshoe vortex can be followed from just downstream of the saddle point to the row of wall jets. The vortex is then pushed along the row of jets and out of the test section without impinging on the suction blade.

#### 6.4 *Velocity Field*

The velocity field was measured in Plane A (location shown in Figure 11) using the LDV system for the case without any flow modifications and for the case with the twelve wall jets. The case without any flow modifications, shown in Figure 35a, shows the horseshoe vortex along the suction side blade. The center of the vortex is located at approximately 60 mm up from the endwall and 25 mm away from the suction wall. The length of the velocity vectors is proportional to the magnitude of the velocity in that direction. The maximum velocity obtained is 13.2 m/s. The suction blade ink dots, shown in Figure 22, shows the upward flow of the vortex from approximately 5 - 60 mm up from the endwall. This corresponds to the upward flow of the vortex illustrated by the velocity field.

In the case with the twelve wall jets operating, the horseshoe vortex was moved, as shown in Figure 36a. The center of the vortex is located approximately 70 mm up from the endwall and 37 mm away from the suction wall. The length of the velocity vectors is less than the length for the vectors in the case without any flow modifications. This shows that the horseshoe vortex is not as strong as in the case without jets. The maximum velocity for the case with jets is 9.2 m/s. The suction blade ink dots, shown in Figure 32, agree with the velocity field. The area on the suction blade from the endwall to 30 mm up the blade shows low shear stresses on the ink dots indicated by the traces parallel to the endwall. The upward motion of the vortex, shown by the velocity field in the region between 30 mm and 70 mm up the suction blade, corresponds to the inclined ink traces in that same region on the suction side blade. The inclination of the ink trace in the case with

less than the inclination in the case without jets. This indicates that the horseshoe vortex is weaker in the case without the jets and further from the suction side wall.

### 6.5 *Aerodynamic Pressure Losses*

An analysis of the aerodynamic pressure losses in Plane A (location shown in Figure 11) was done by obtaining total pressures with the Kiel probe. The results for the case without any flow modifications is shown in Figure 35b along with the corresponding velocity field. Color is proportional to total pressure loss coefficient,  $C_{p_t}$ , as defined in Equation (3). Dark blue represent low  $C_{p_t}$  while red indicates high  $C_{p_t}$ . It is clearly indicated by the light blue region (maximum  $C_{p_t} = 0.9363$ ) that high aerodynamic pressure losses correspond to the center of the horseshoe vortex. This result was expected and agrees with Chung's (1992) study.

The results from the case with the twelve jets in operation is shown in Figure 36b along with the corresponding velocity field. It shows that the center of the horseshoe vortex corresponds to the region of high aerodynamic pressure losses. It was expected that the pressure losses in the case with the jets would be lower than the case without jets. The velocity field and blade ink dots indicate that the shear stresses on the suction side blade due to the vortex are much smaller in the case with the jets. The velocity field also indicates that the strength or velocity of the horseshoe vortex is smaller for the case with the jets. The expectation is proven wrong by the yellow and red region corresponding to the location of the horseshoe vortex. These colors indicate high pressure losses as high as

$C_{p_t} = 1.2055$ . These aerodynamic losses degrade the turbine performance thus decreasing the efficiency.

With the use of the full fence, modeled after Chung (1992), the aerodynamic pressure losses were decreased as shown in Figure 37. This figure also shows that the fence moved the horseshoe vortex towards the endwall and away from the suction side blade. These are the same results arrived at by Chung (1992). Therefore, the wall jets were not as effective as the fence was in reducing the aerodynamic pressure losses in the turbine passage.

## 7 CONCLUSIONS

---

1. A two half-blade test section was used to successfully model the passage flow in an actual turbine.
2. The installation of wall jets downstream of the saddle point, near the leading edge of the pressure side blade proved to be ineffective in diverting the path of the horseshoe vortex.
3. The model fence used in this study had similar effects on the diversion of the horseshoe vortex to the fence used by Chung (1992).
4. The fence was then modified in order to minimize the number of wall jets in the endwall necessary to divert the path horseshoe vortex. This modified fence was effective in diverting the path of the horseshoe vortex and reducing its effect on the suction side blade.
5. Twelve wall jets operating at a blowing ratio of 1.7 successfully diverted the path of the horseshoe vortex, thus reducing its effect on the suction side blade. This should allow for improved film cooling in that area which would then allow for higher inlet temperatures to the turbine. Higher inlet temperatures would increase the efficiency of the gas turbine engine.

6. The jets had a detrimental effect on the total pressure losses, increasing the aerodynamic losses in the passage. This would decrease the efficiency of the gas turbine engine.
  
7. Further experiments must be conducted in order to conclude whether or not the twelve wall jets would have an overall favorable effect on the efficiency of the gas turbine engine.

## REFERENCES

---

- Chen, P.H., 1988, "Measurement of Local Mass Transfer from a Gas Turbine Blade." Ph.D. Thesis, Department of Mechanical Engineering, University of Minnesota, Minneapolis, MN.
- Chen, P.H. and Goldstein, R.J., 1991, "Convective Transport Phenomena on the Suction Surface of a Turbine Blade including the influence of Secondary Flows Near the Endwall." ASME paper 91-GT-35.
- Chung, J.T., 1992, "Flow and Heat Transfer Experiments in the Turbine Airfoil/Endwall Region." Ph.D. Thesis, Department of Mechanical Engineering, University of Minnesota, Minneapolis, MN.
- Chung, J.T. and Simon, T.W., 1990, "Three-Dimensional Flow Near the Blade/Endwall Junction of a Gas Turbine: Visualization in a Large-Scale Cascade Simulator." ASME paper 90-WA/HT-4.
- Chung, J.T. and Simon, T.W., 1993, "Effectiveness of the Gas Turbine Endwall Fences in Secondary Flow Control at Elevated Freestream Turbulence Levels." ASME paper 93-GT-51.
- Chung, J.T. and Simon, T.W. and Buddhavarapu, J., 1991, "Three-Dimensional Flow Near the Blade/Endwall Junction of a Gas Turbine: Application of a Boundary Layer Fence." ASME paper 91-GT-45.
- Chyu, M.K. and Hsing, Y.C. and Bunker, R.S., 1998, "Measurements of Heat Transfer Characteristics of Gap Leakage Around a Misaligned Component Interface." ASME paper 98-GT-132.
- Dossena, V. and Perichizzi, A. and Savini, M., 1998, "The Influence of Endwall Contouring on the Performance of a Turbine Nozzle Guide Vane." ASME paper 98-GT-71.
- Duden, A. and Raab, I. and Fottner, L., 1998, "Controlling the Secondary Flow in a Turbine Cascade by 3D Airfoil Design and Endwall Contouring." ASME paper 98-GT-72.
- Flack, K.A., 1998, "Laser Doppler Anemometry." EM 324 Class notes.
- Goldstein, R.J. and Spores, R.A., 1988, "Turbulent Transport on the Endwall in the Region Between Adjacent Turbine Blades." ASME Journal of Heat Transfer. Vol. 110, pp. 892-869.

Ito, S., 1978, "Film Cooling and Aerodynamic Loss in a Turbine Cascade." Ph.D. Thesis. Dept. of Mechanical Engineering, University of Minnesota, Minneapolis, MN.

Lakshminarayana, B., 1996, Fluid Dynamics and Heat Transfer of Turbomachinery. John Wiley & Sons, Inc., pp. 144, 149.

Langston, L.S. and Boyle, M.T., 1982, "A New Surface-Streamline Flow Visualization Technique." *Journal of Fluid Mechanics*, Vol 125, pp. 53-57.

Langston, L.S. and Nice, M.L. and Hooper R.M., 1977, "Three-Dimensional Flow Within a Turbine Cascade Passage." *Journal of Engineering for Power*, Vol. 99, pp. 21-28.

Ligrani, P.M. and Mitchell, S.W., 1994, "Interaction Between Embedded Vortices and Injectant From Film Cooling Holes With Compound Angle Orientations in a Turbulent Boundary Layer." *Journal of Turbomachinery*, Vol. 116, January 1994.

Michelassi, V. and Martelli, F. and Corradini, U., 1998, "Secondary Flow Decay Downstream of Turbine Inlet Guide Vane with Endwall Contouring." ASME paper 98-GT-95.

Qiu, S. and Simon, T.W., 1998, Private Communication.

Stoddard, R.M., 1998, "Wind Tunnel Qualification Tests." Engineering and Weapons Report: EW-03-98, pp. 2-27.

Volino, R.J. and Simon, T.W., 1995, "Measurements in Transitional Boundary Layers Under High Free-Stream Turbulence and Strong Acceleration Conditions." NASA Contractor Report 198413, p. 24.

White, F.M., 1994, Fluid Mechanics, Third Edition. McGraw-Hill, Inc., pp. 156-158, 258, 394-396.

Yeh, F.C. and Gladden, H.J., 1989, "Experience with Advanced Instrumentation in a Hot section Cascade." ASME paper HTD Vol. 119, pp. 69-80.

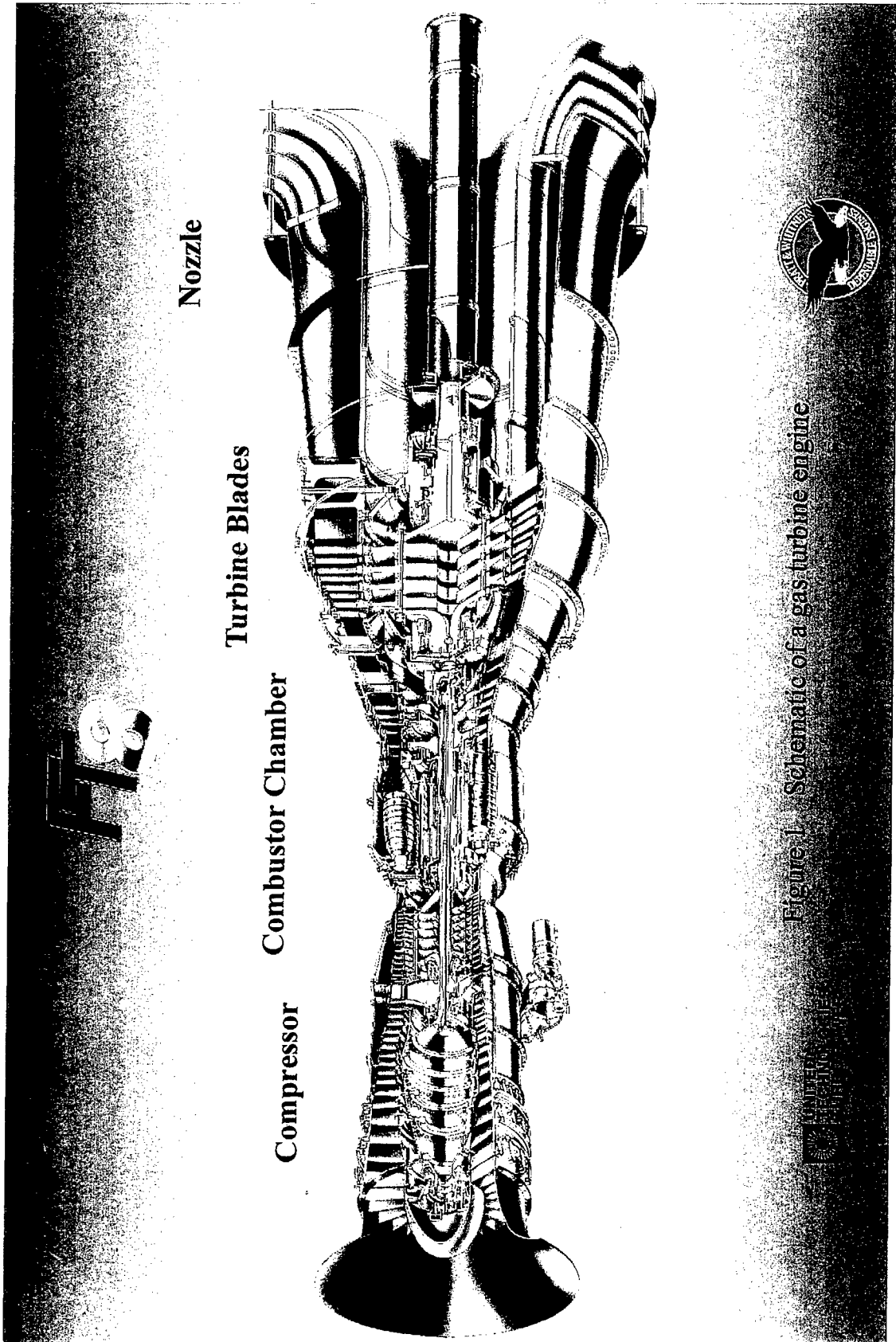


Figure 1 Schematic of a gas turbine engine

SAE

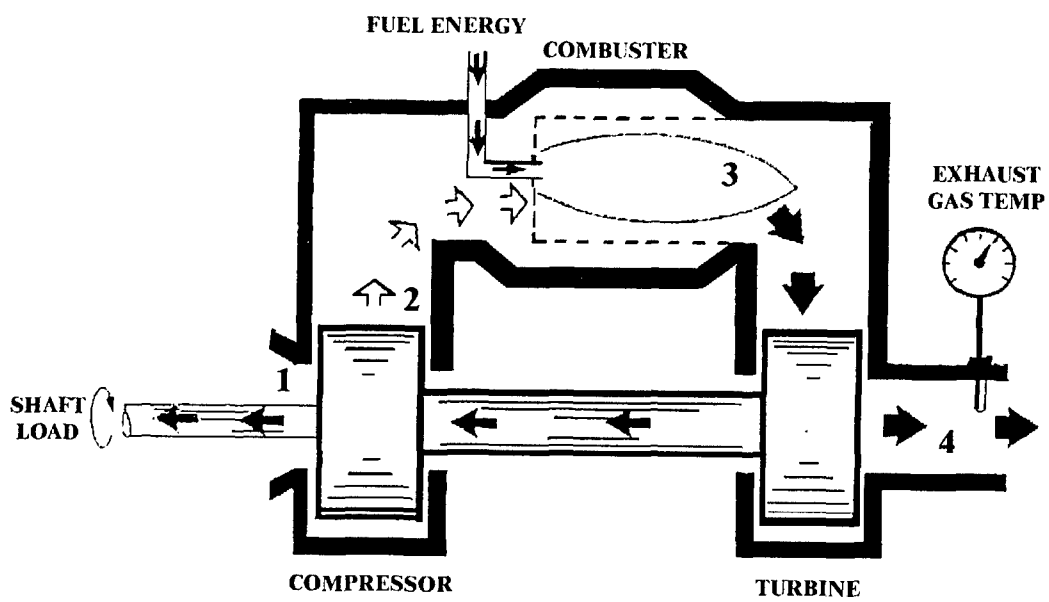


Figure 2 Gas Turbine Schematic

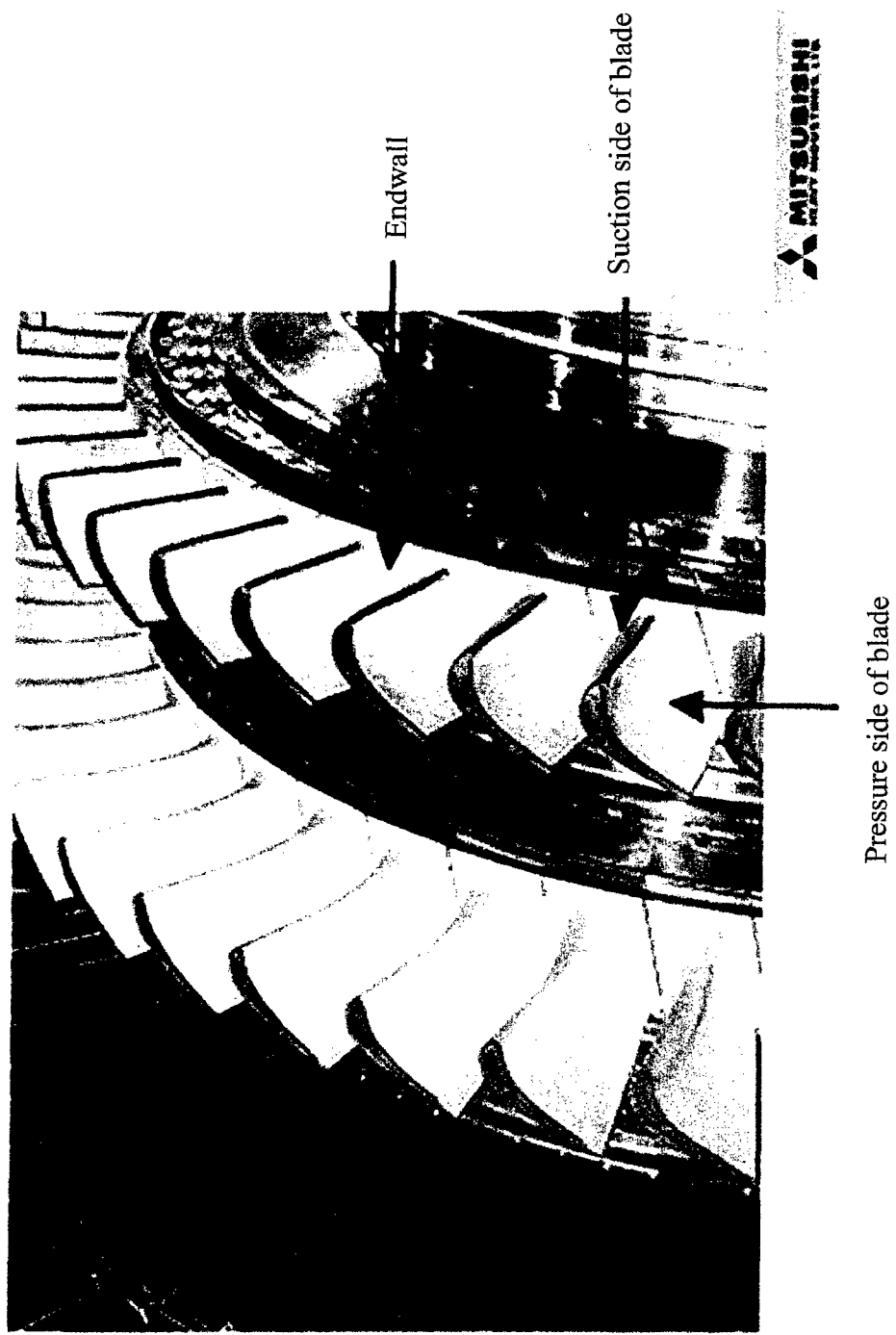


Figure 3 Turbine blade and endwall configuration

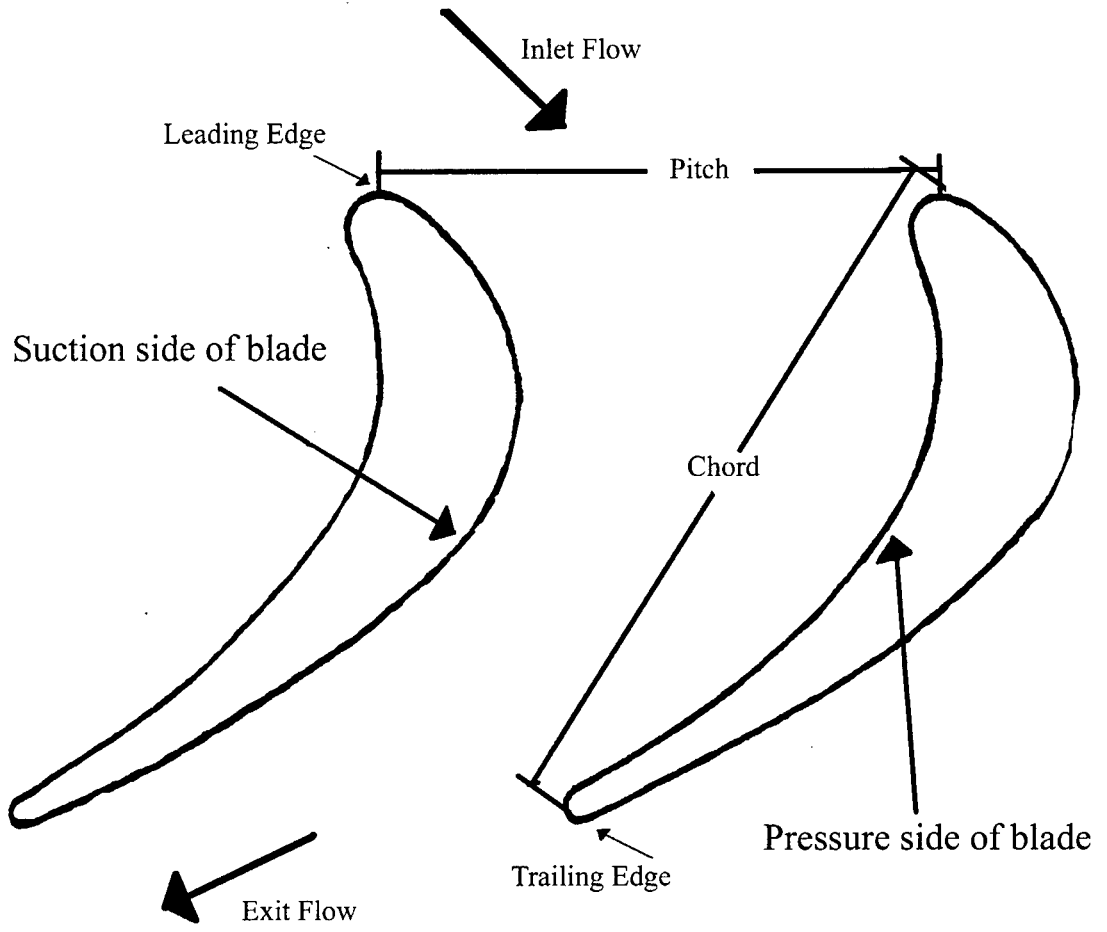


Figure 4 Terminology associated with turbine passage

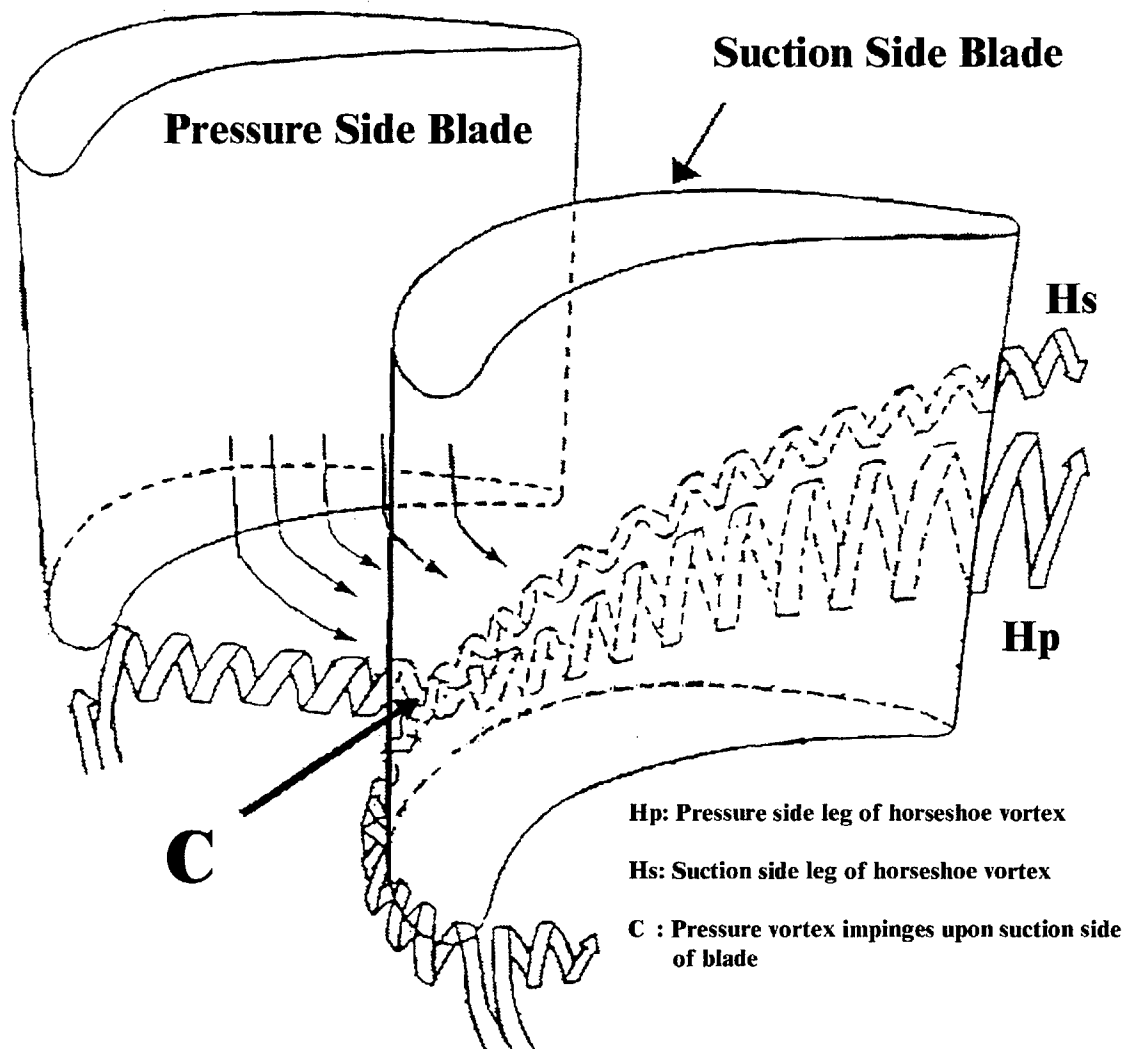


Figure 5 Schematic of horseshoe vortex impinging upon suction blade  
(Chen and Goldstein, 1991)

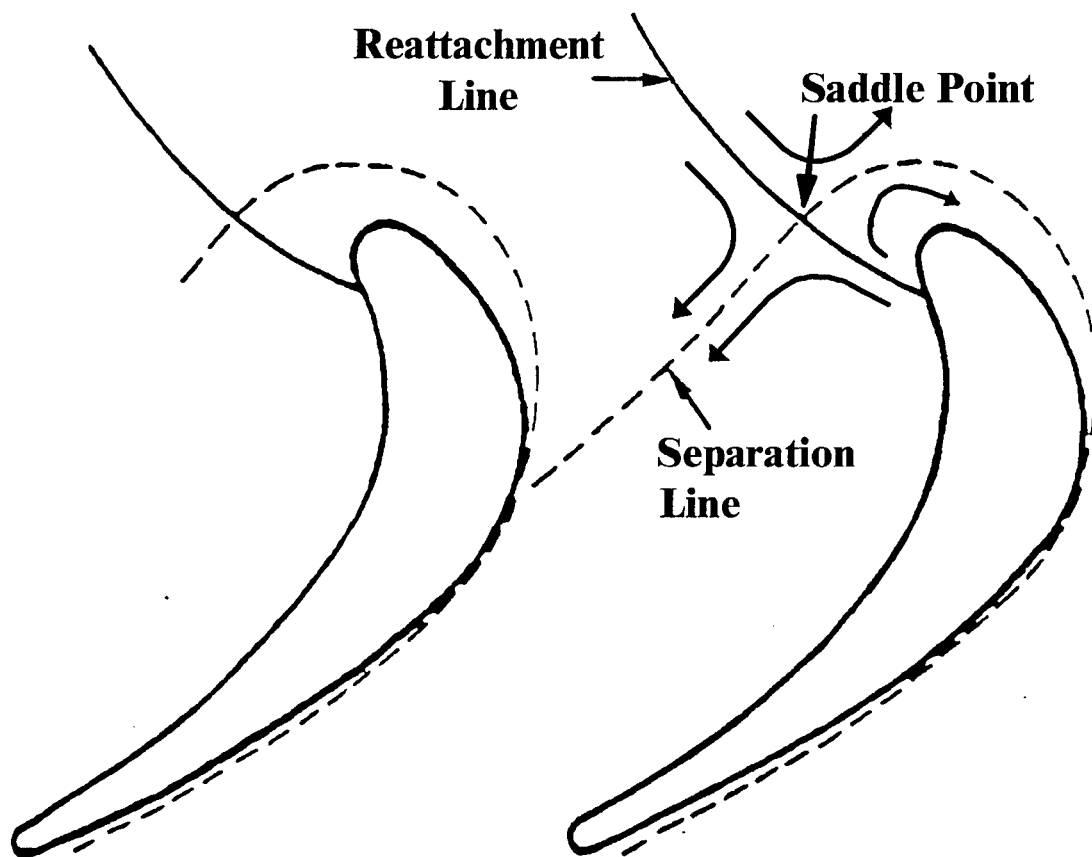


Figure 6 Endwall three-dimensional separation (Langston, 1977)

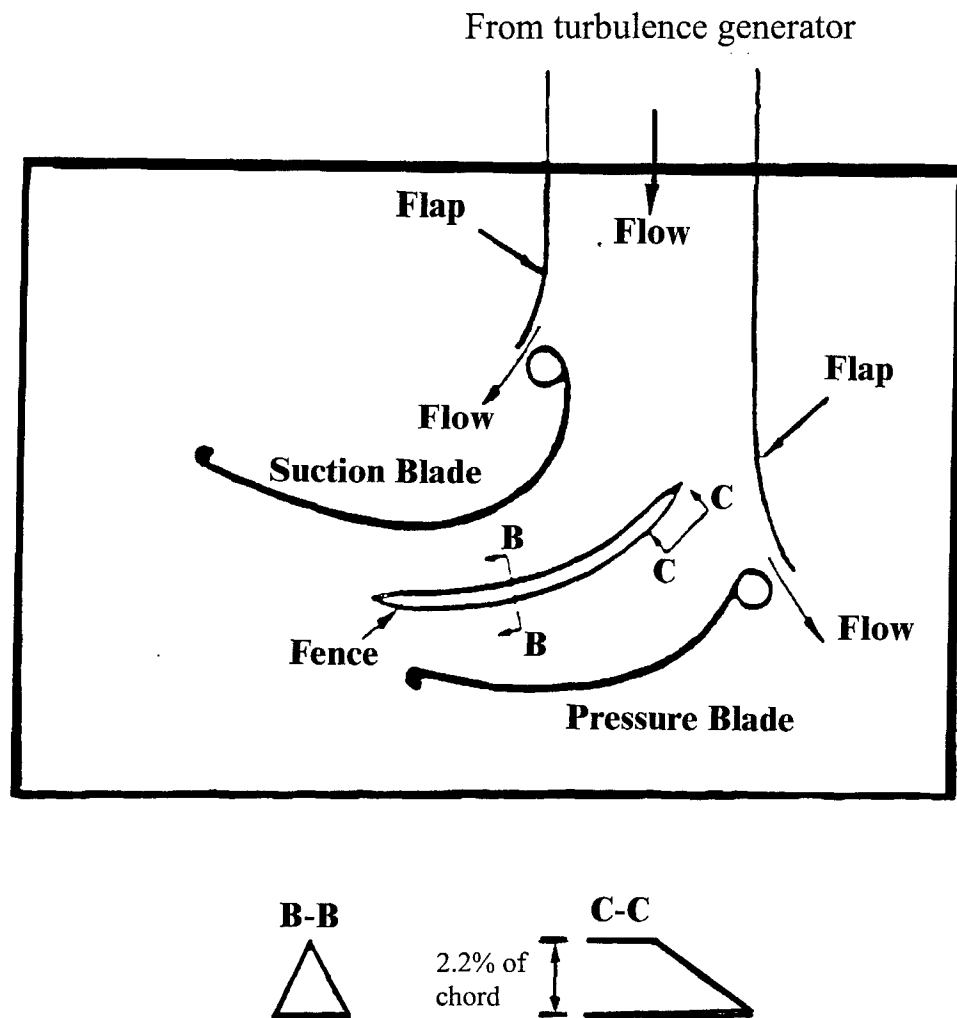


Figure 7 Top view of Chung's test section with fence (Chung, 1992)

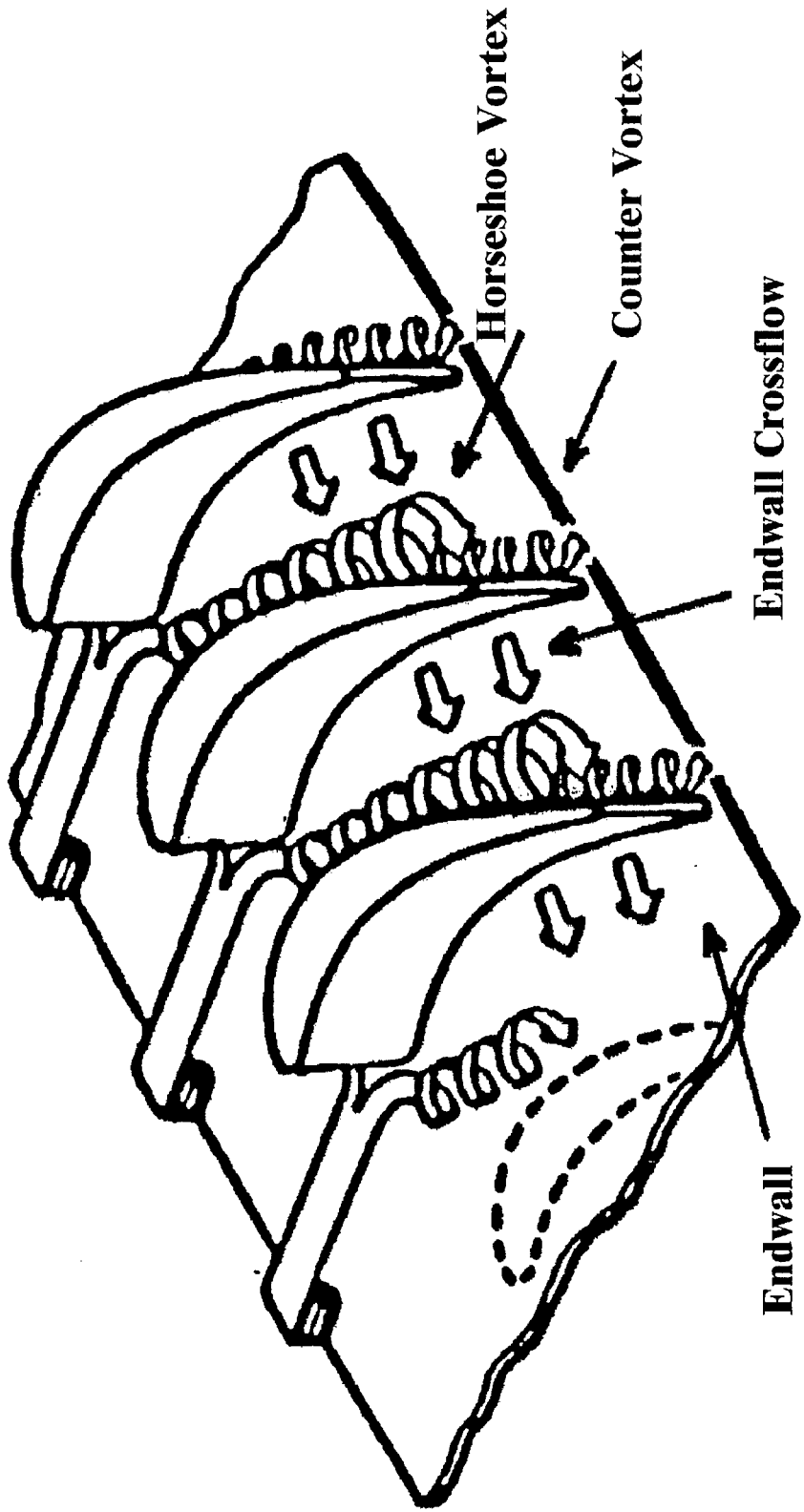


Figure 8 Endwall secondary flow in a turbine cascade

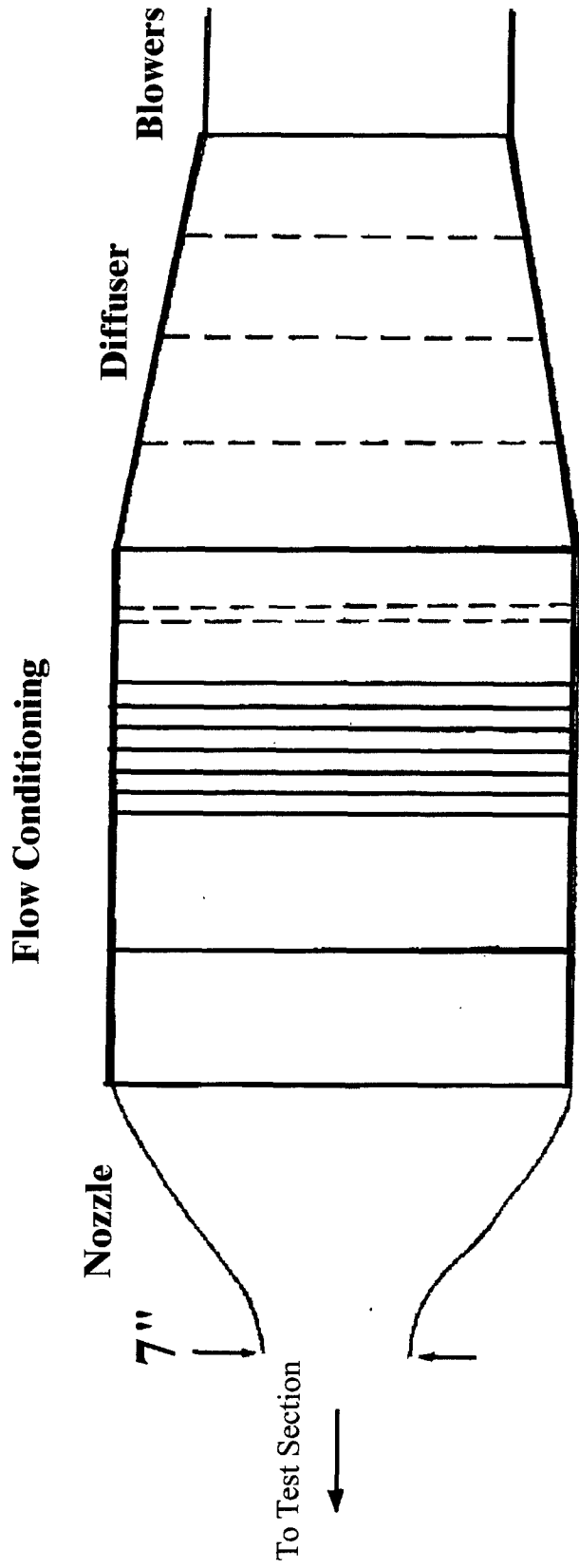


Figure 9 Top view of wind tunnel

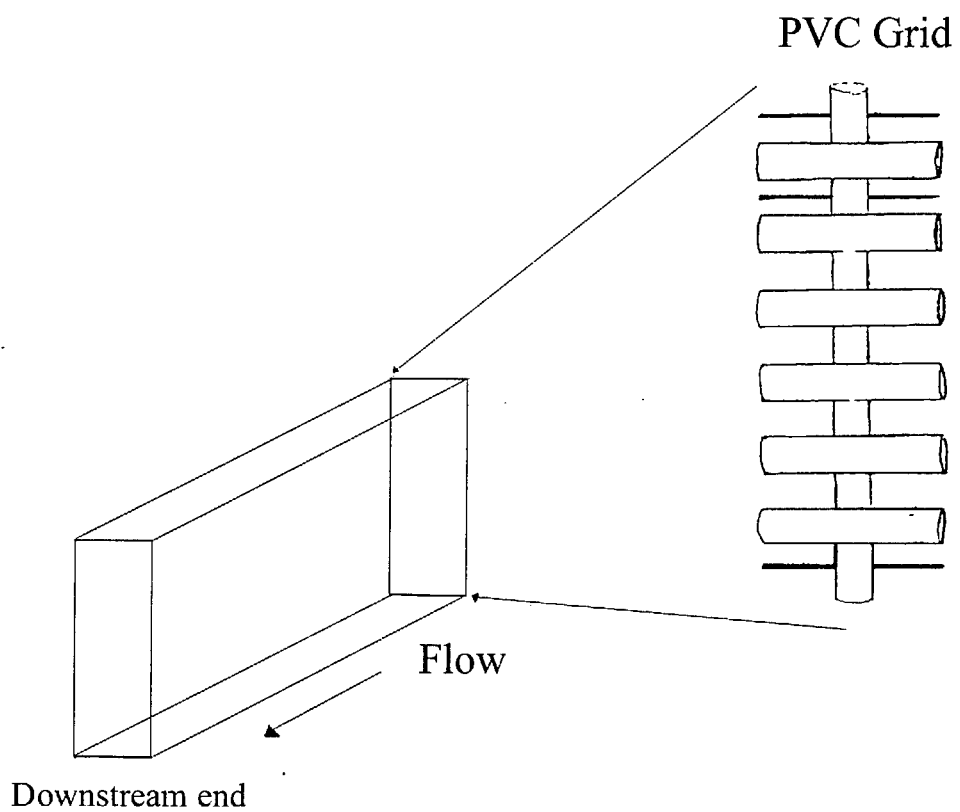


Figure 10 Schematic of turbulence generator (Stoddard, 1998)

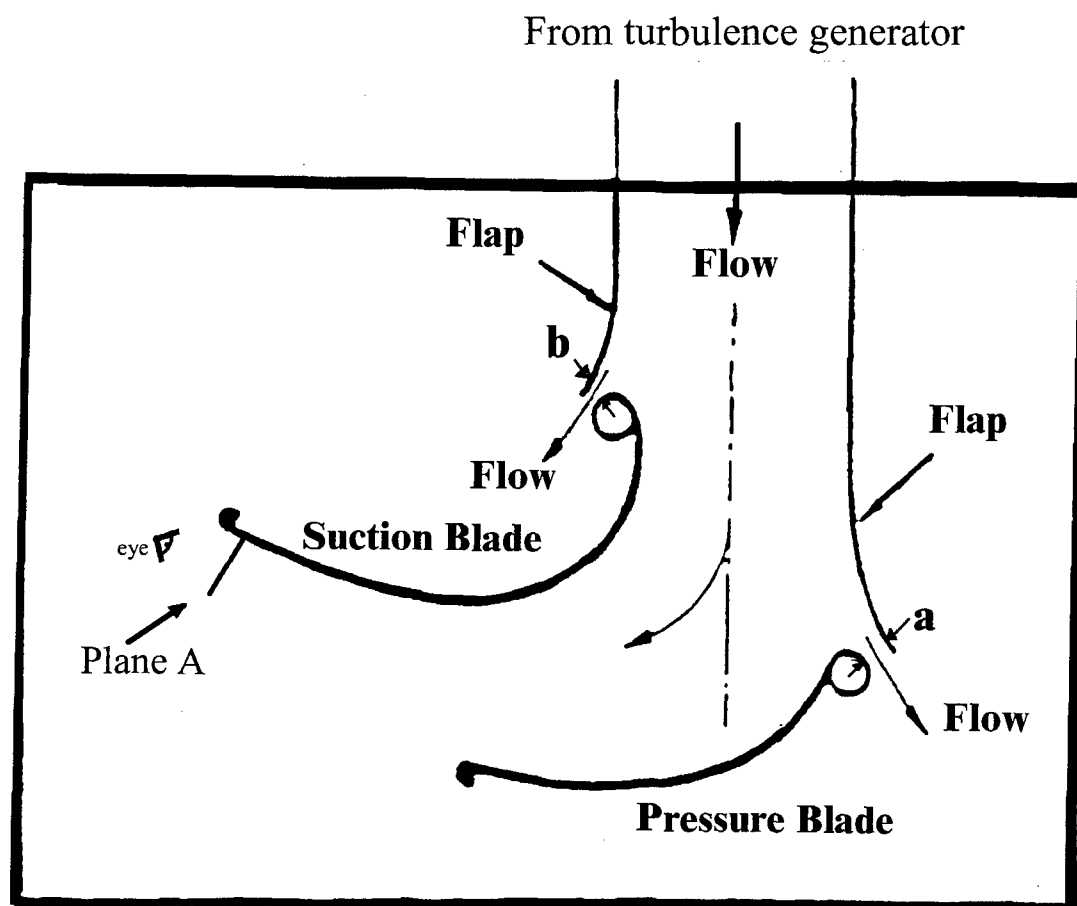


Figure 11 Top view of test section (Chung, 1992)

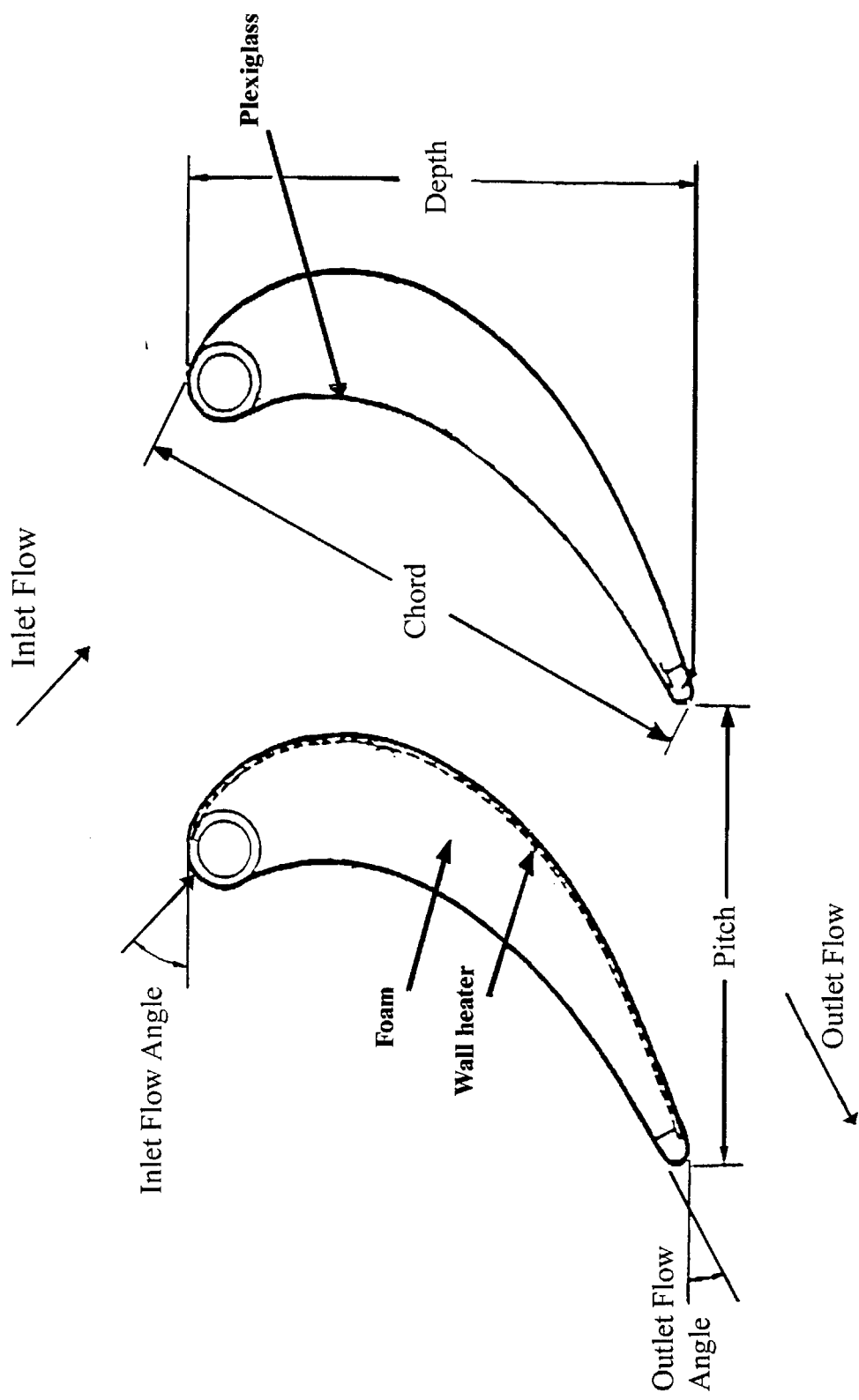


Figure 12 Blade profile and dimension definitions (Chung, 1992)

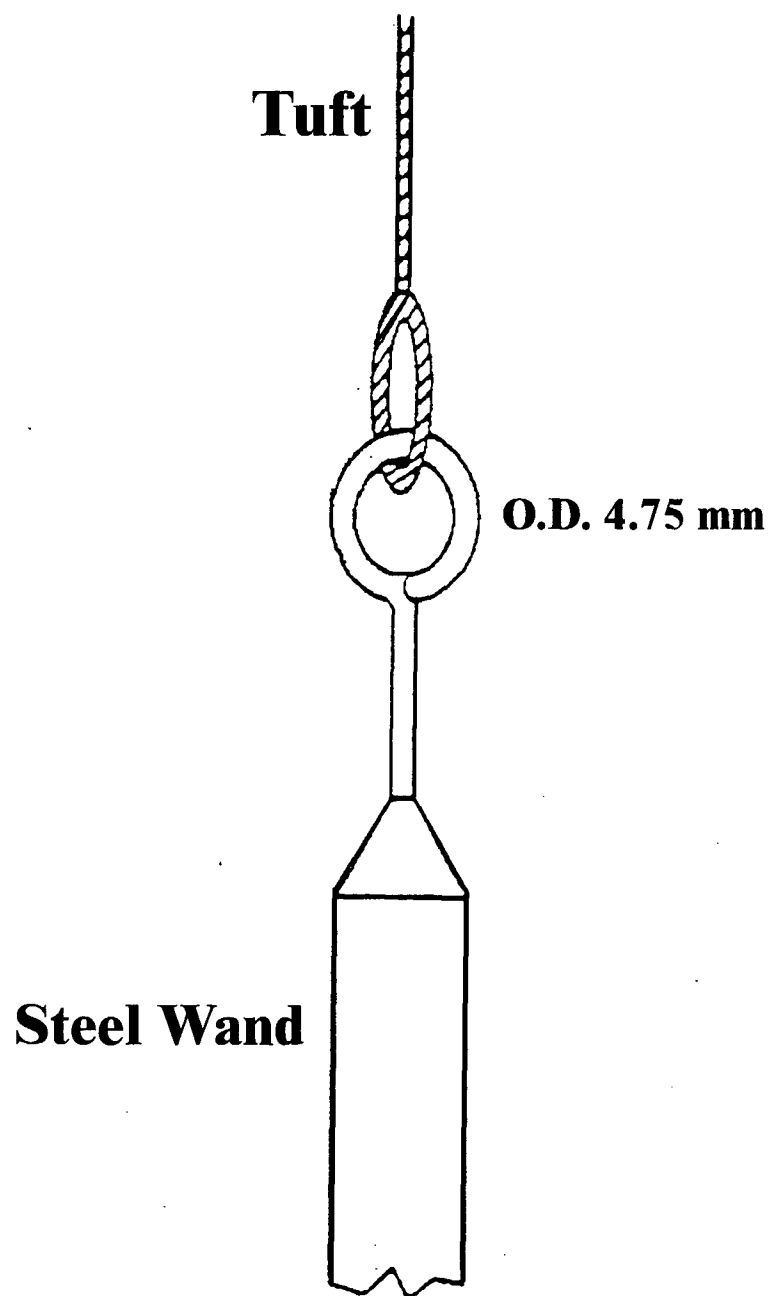


Figure 13 Schematic of single tuft probe (Chung, 1992)

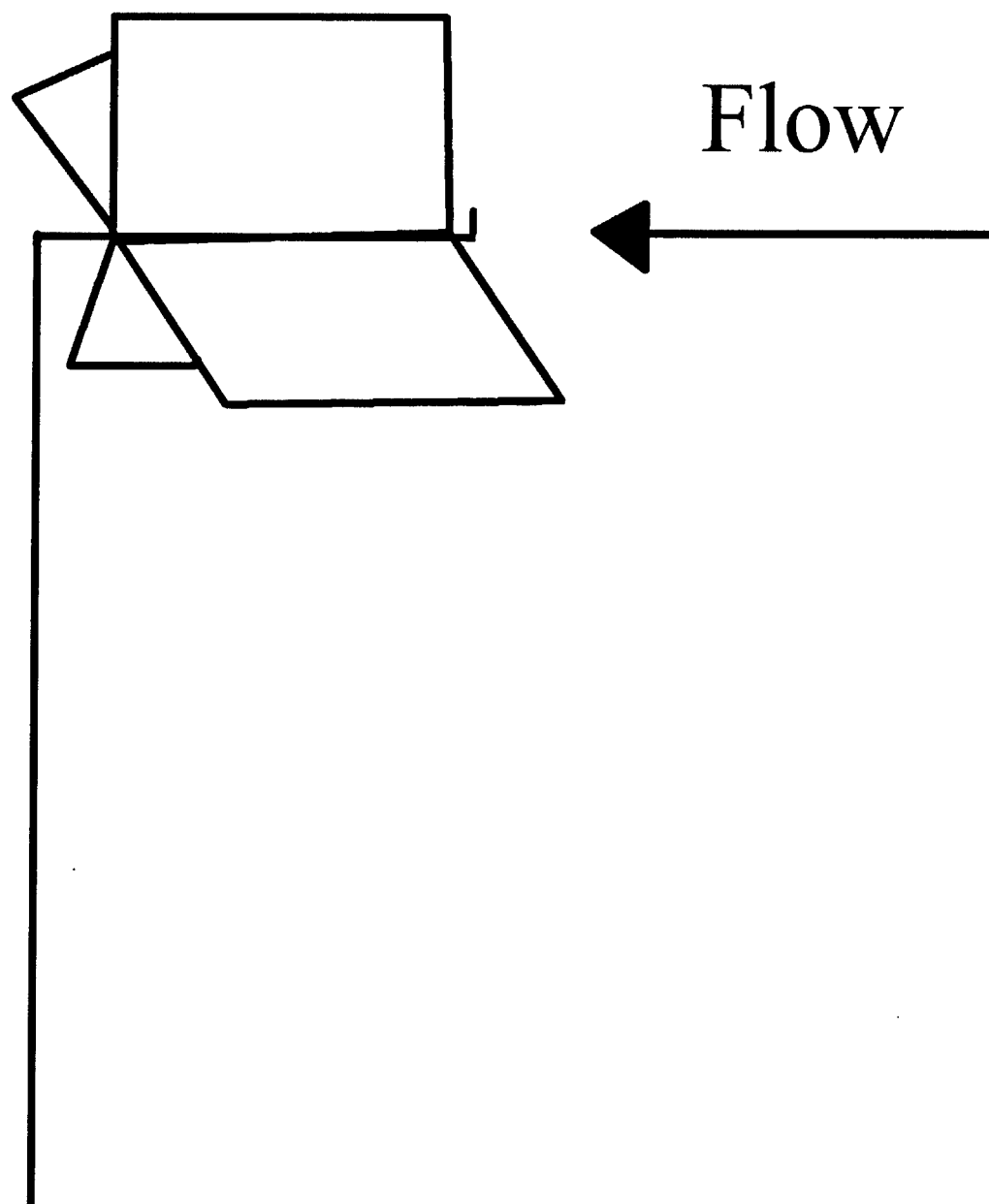


Figure 14 Schematic of vorticity detector

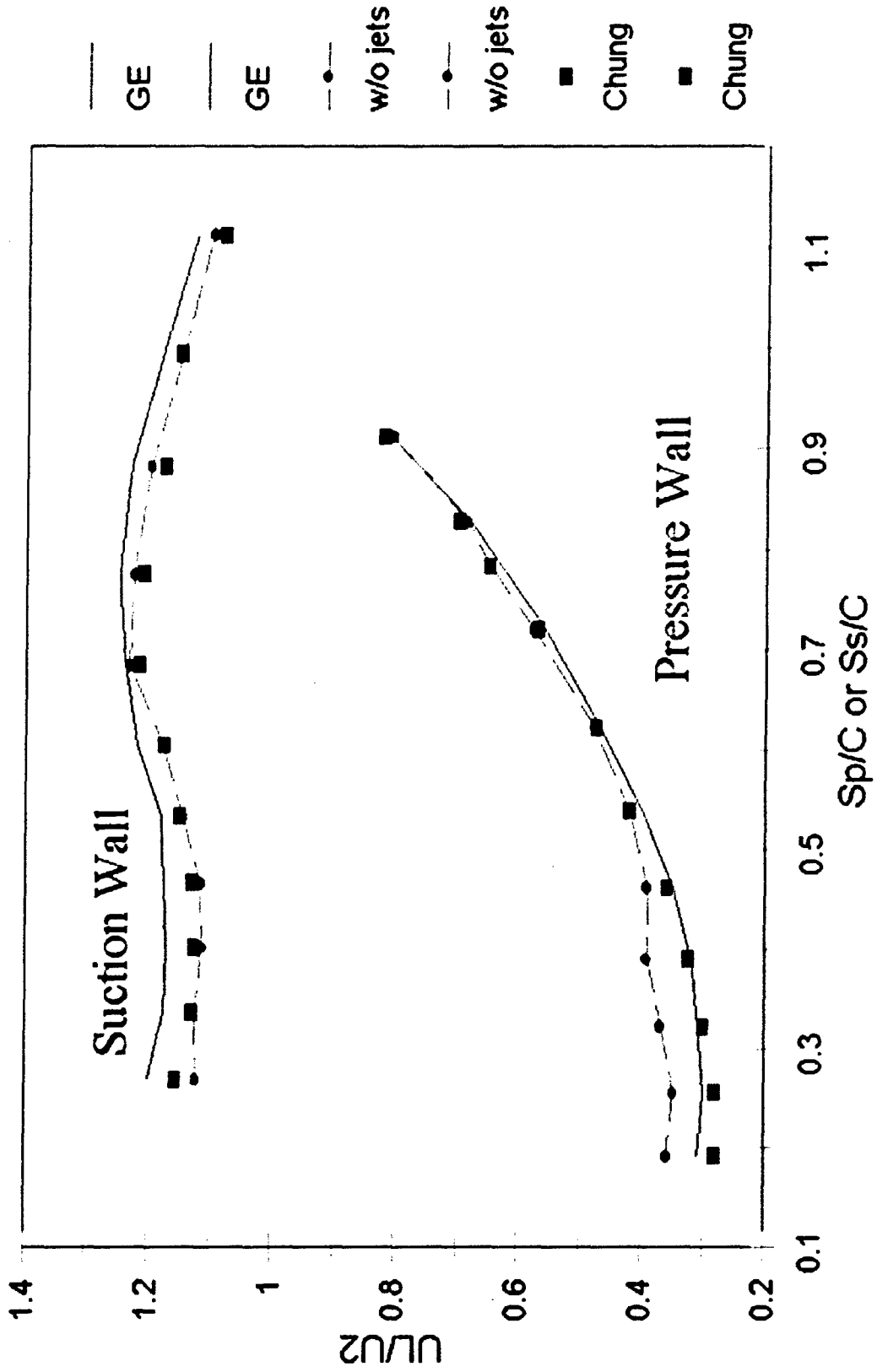


Figure 15 Normalized velocity distribution along the blade surface with no wall jets



Figure 16 Ink dot traces on the endwall - Chung (1992)

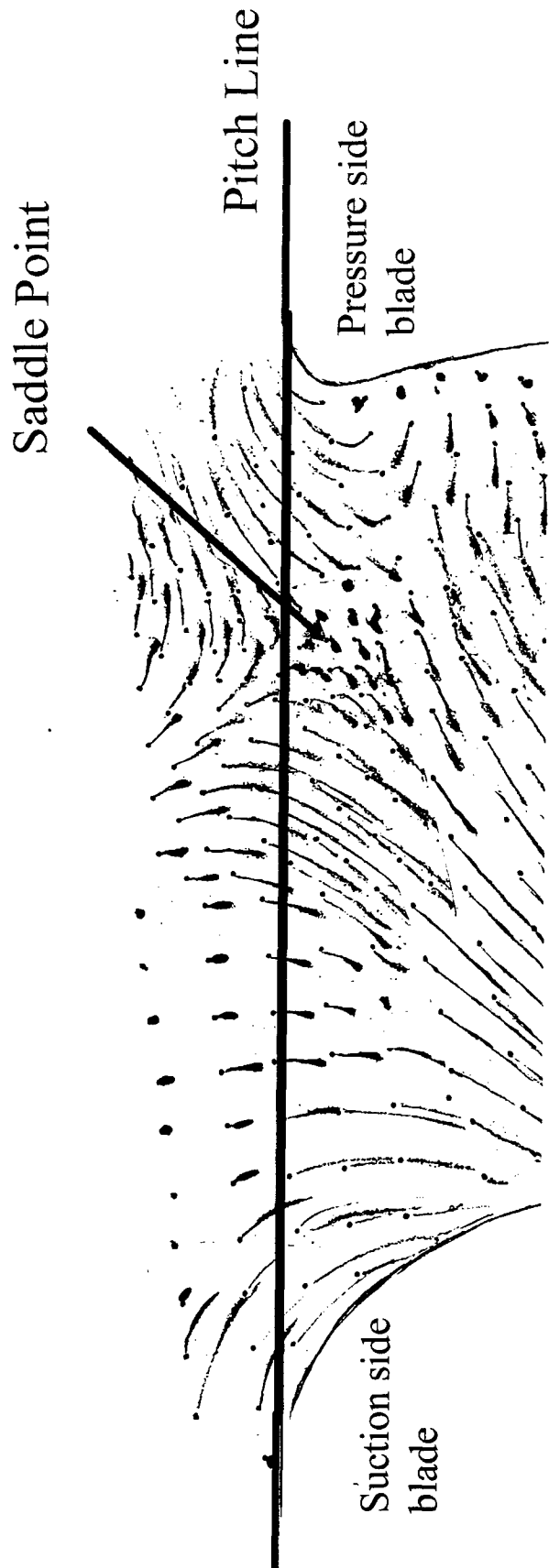


Figure 17 Ink dot traces on the endwall - present study

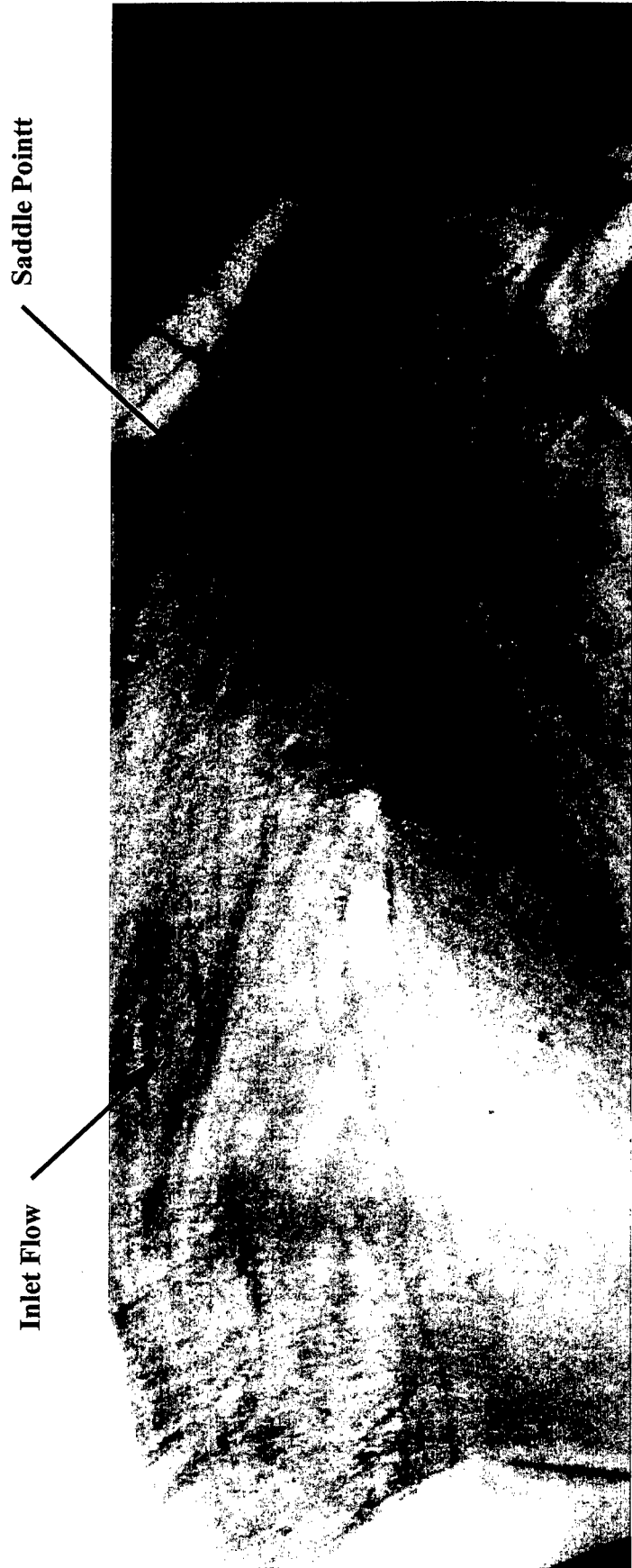


Figure 18 Oil and black powder visualization - present study

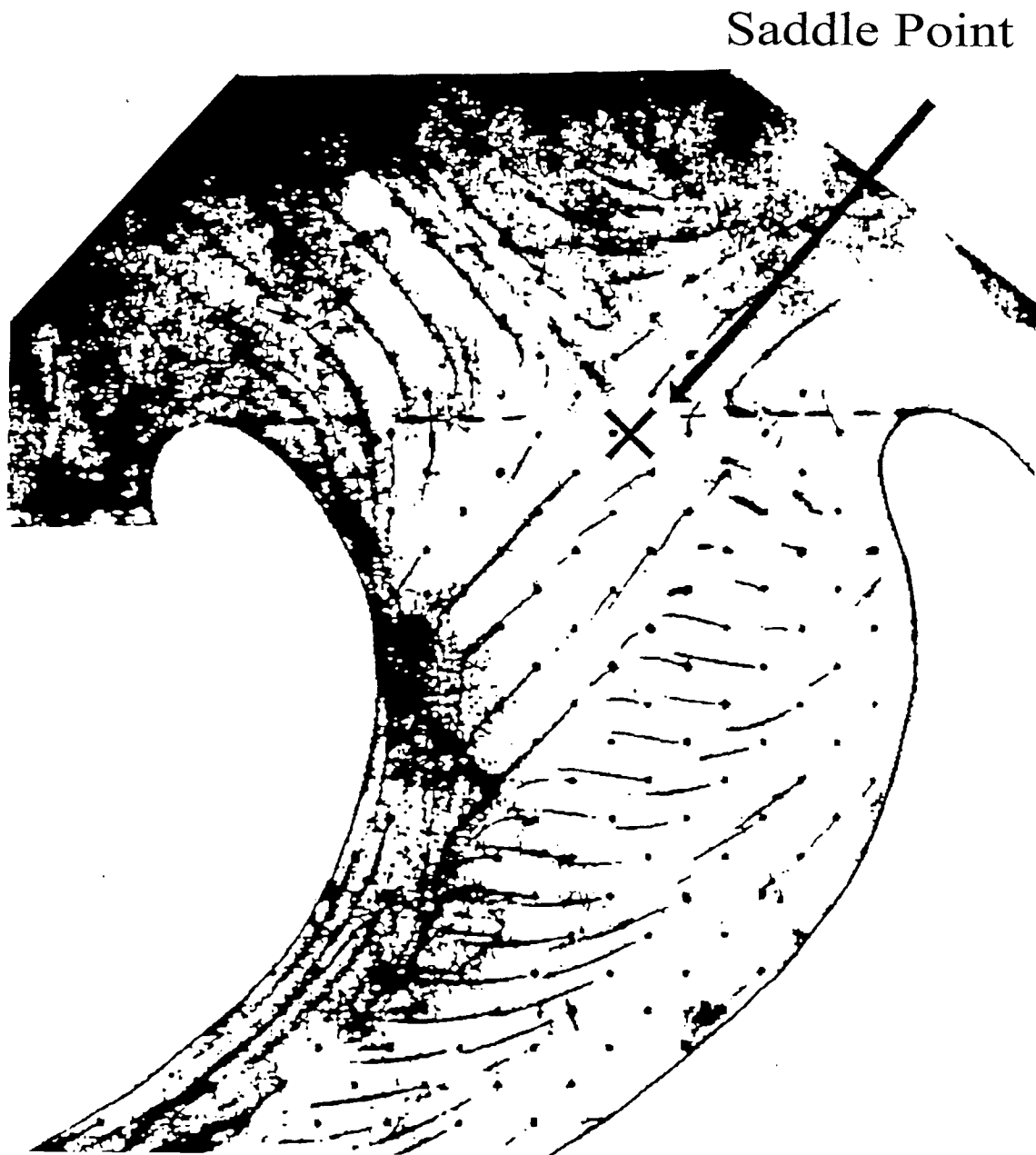


Figure 19 Ink dot traces on the endwall - Chung (1992)

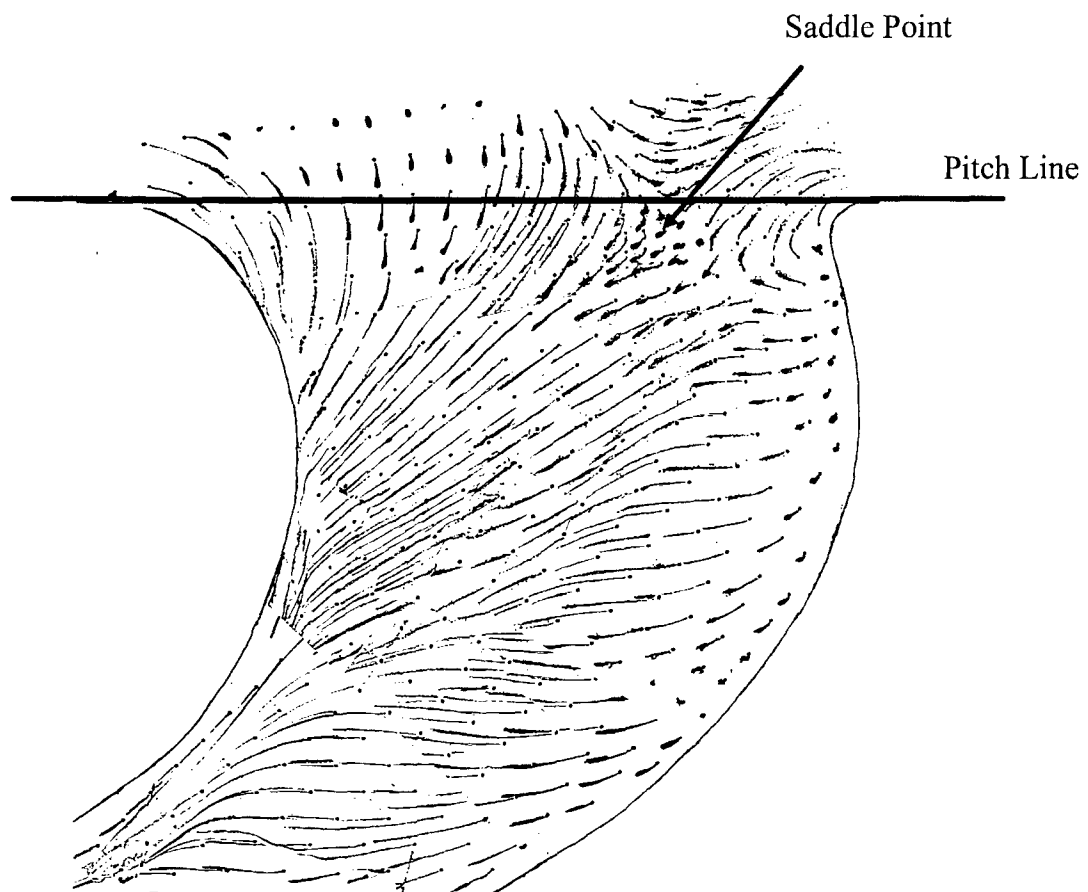
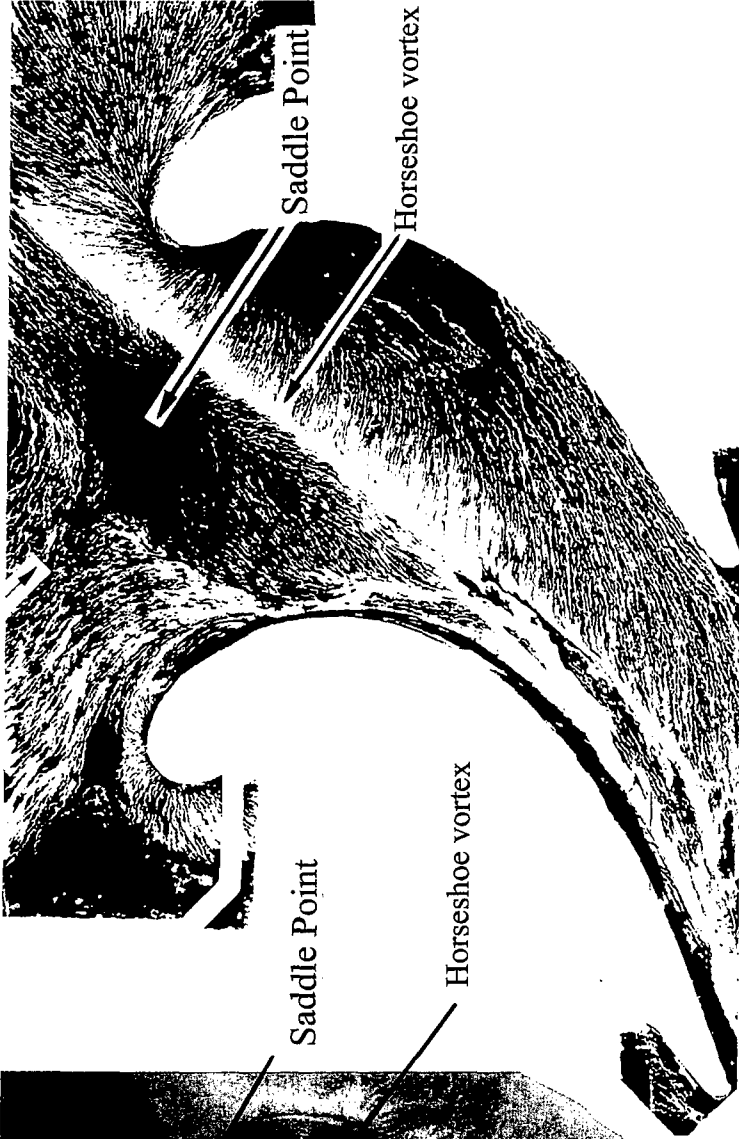


Figure 20 Ink dot traces on the endwall - present study



Present Study



Chung (1992)

Figure 21 Visualization of the endwall shear stress pattern as revealed by oil and blackpowder

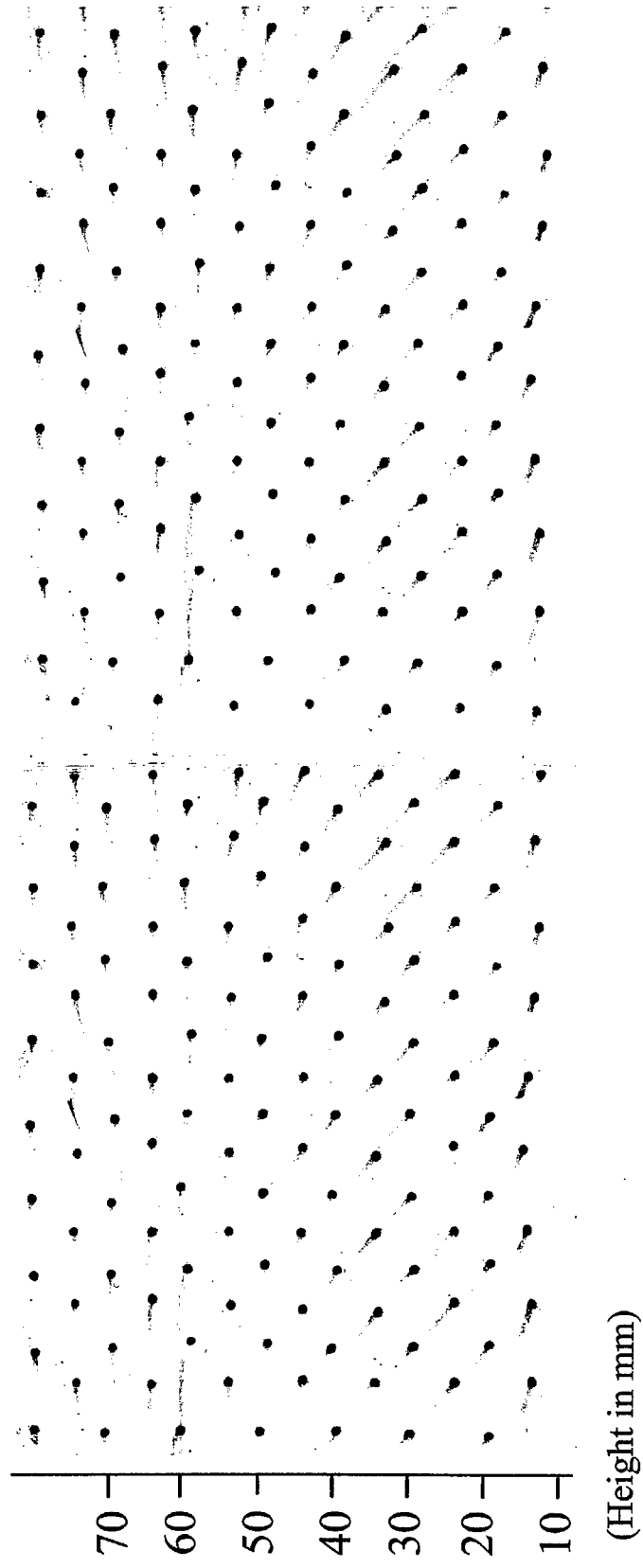


Figure 22 Ink dot flow visualization on the suction blade with no flow modifications

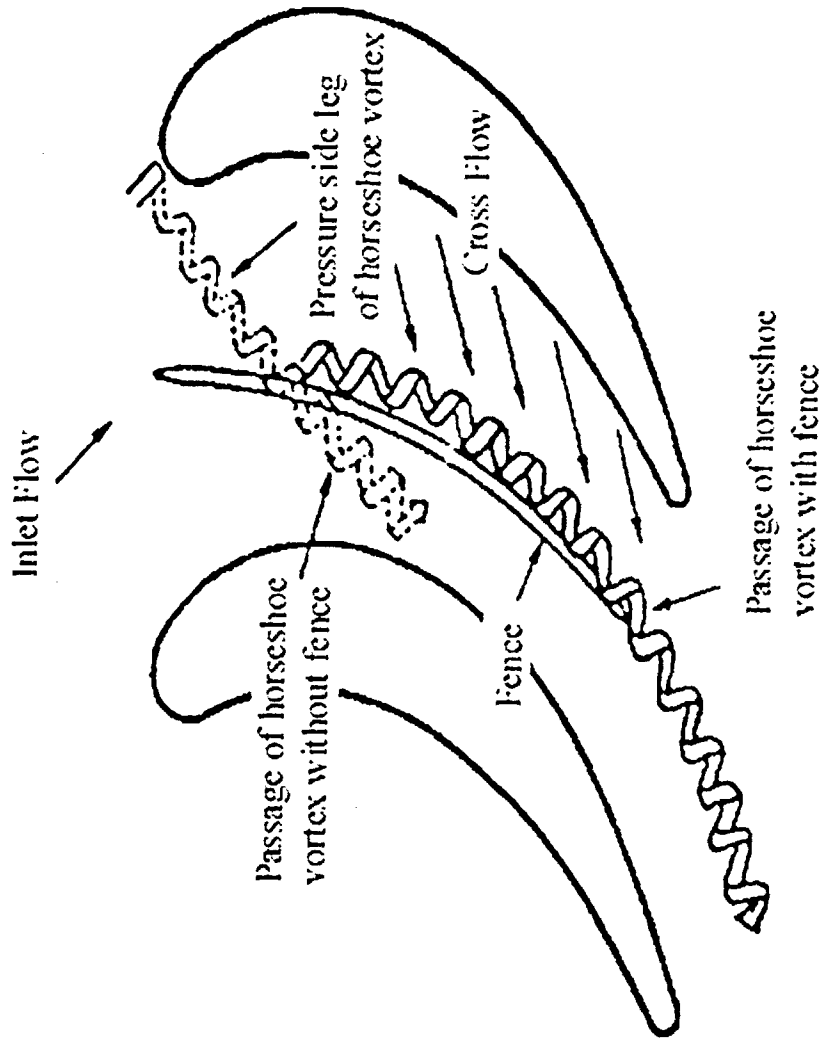


Figure 23 Horseshoe vortex with and without fence  
(Chung, Simon, and Buddhavarapu, 1991)

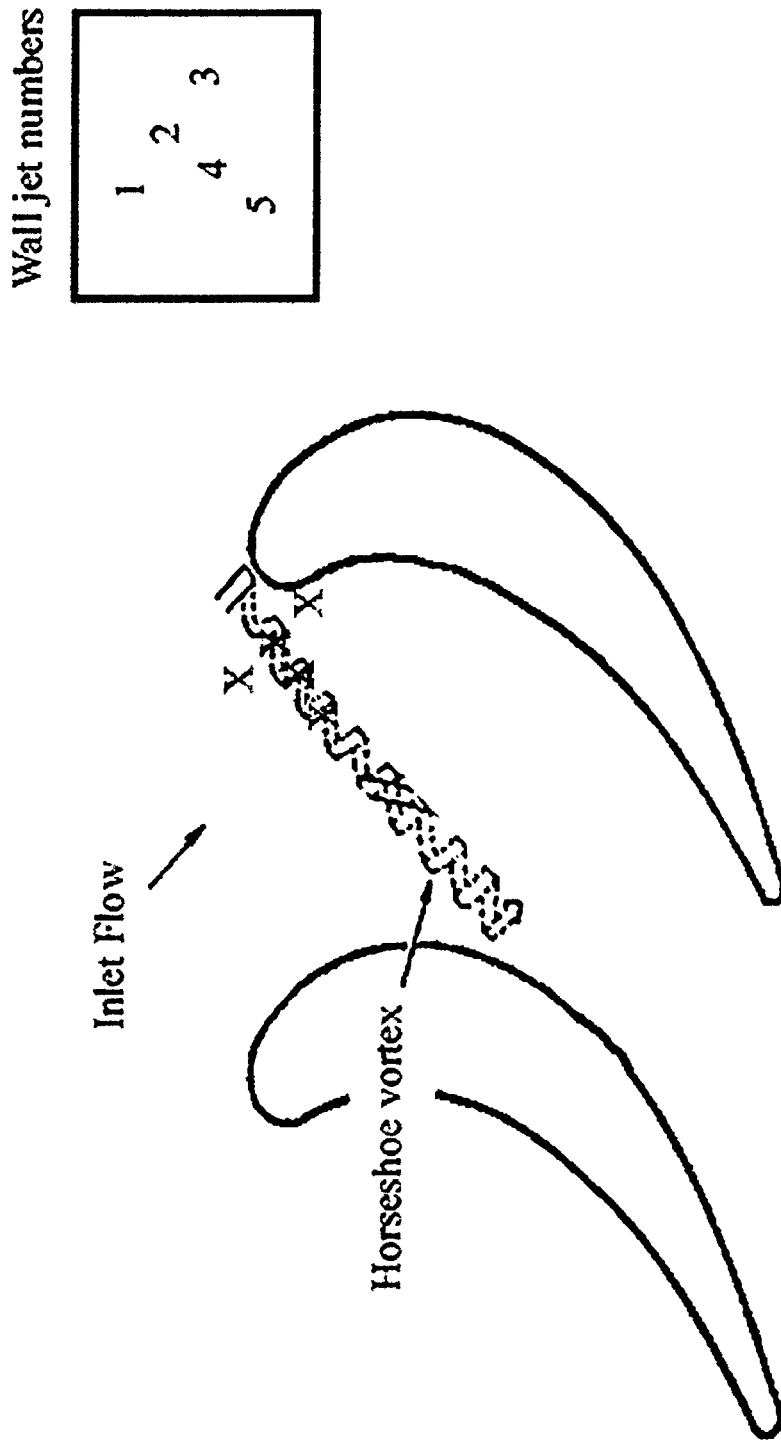


Figure 24 Top view of present test section with jets near the saddle point

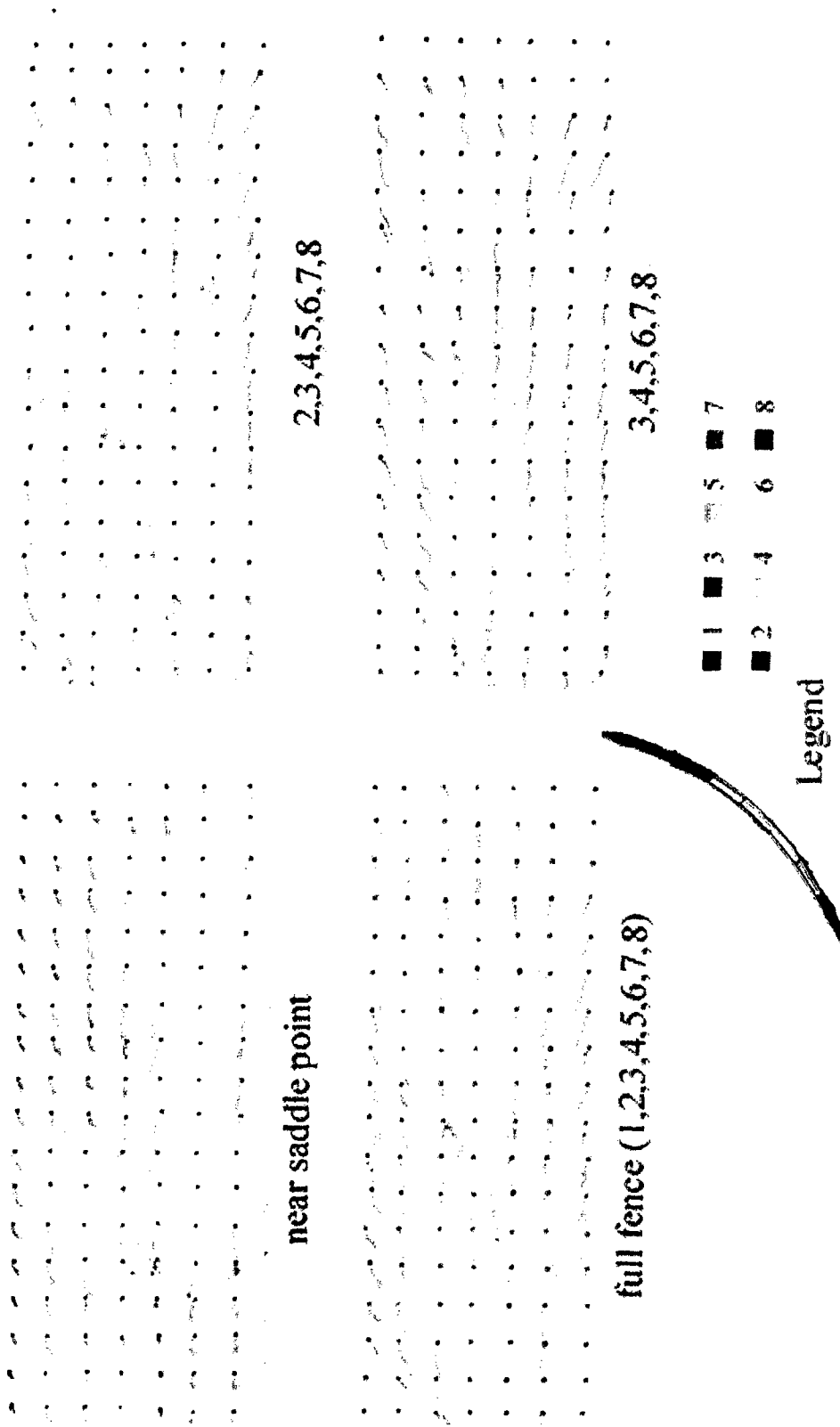


Figure 25 Ink dot flow visualization on the suction side blade

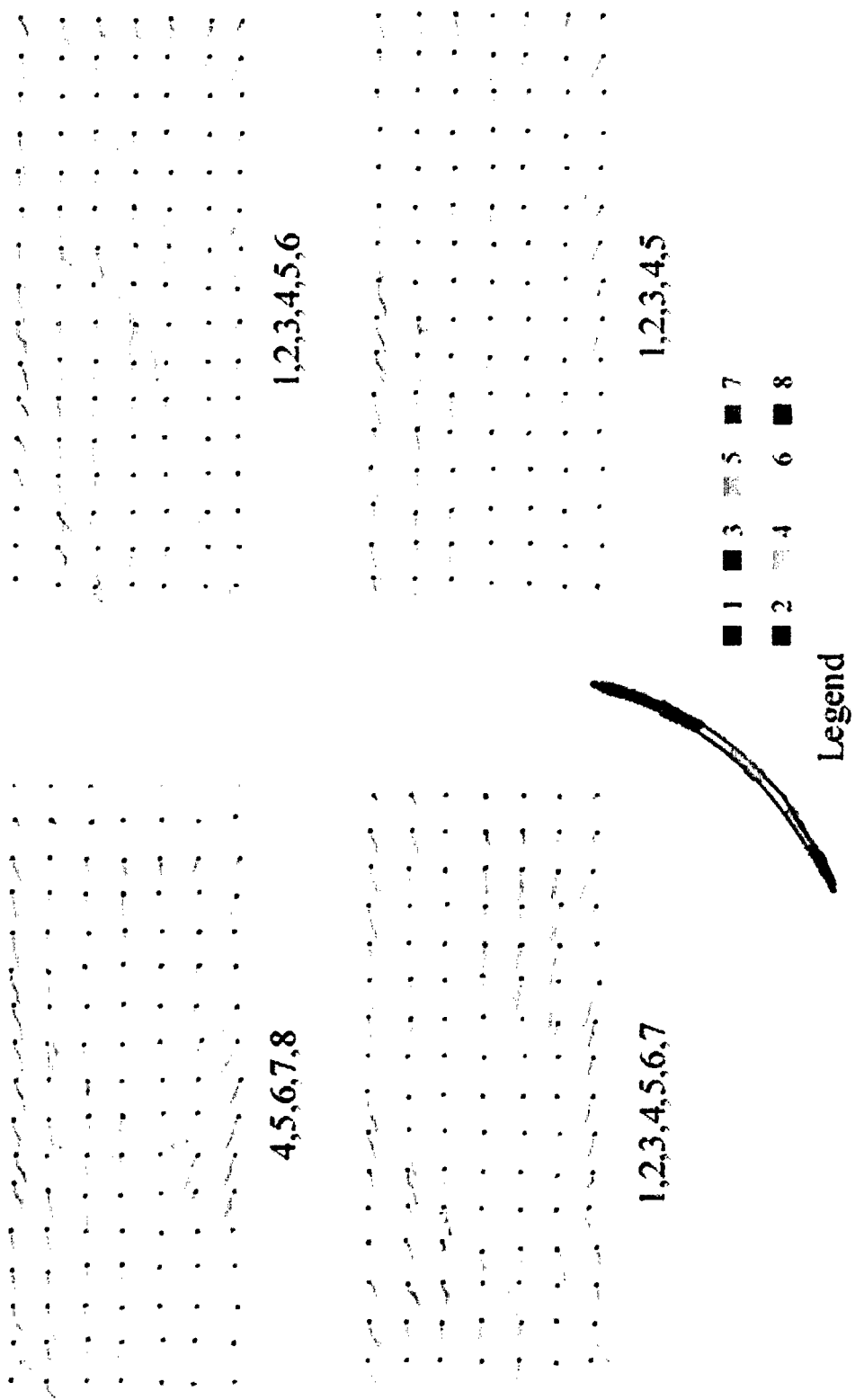
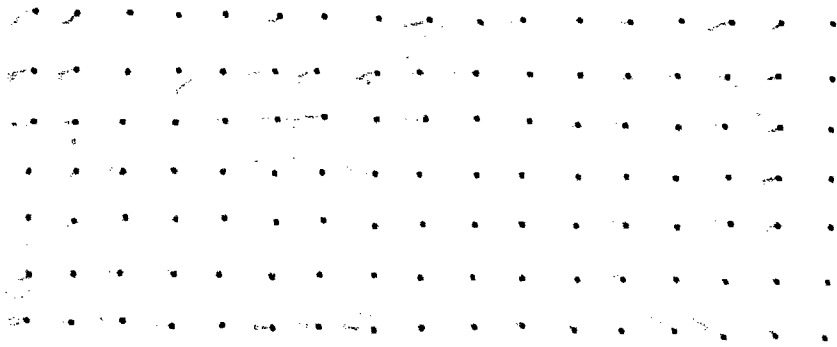
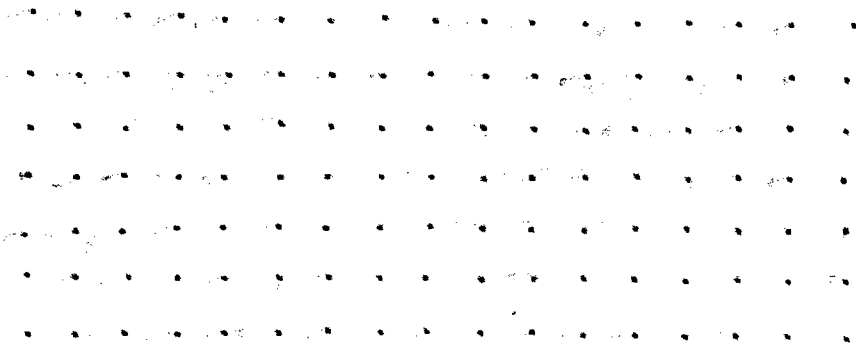


Figure 26 Ink dot flow visualization on the suction side blade



3,4,5,6



3,4,5,6 (modified orientation)



Legend    ■ 3    ● 4    ▣ 5    6

Figure 27    Ink dot flow visualization on the suction side blade

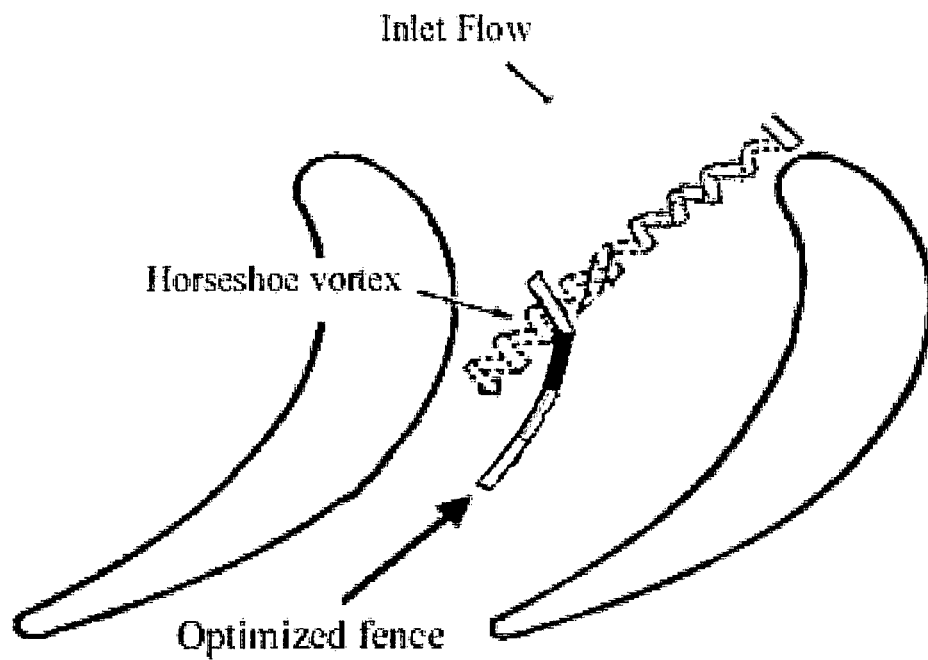


Figure 28 Top view of present test section with modified fence in place

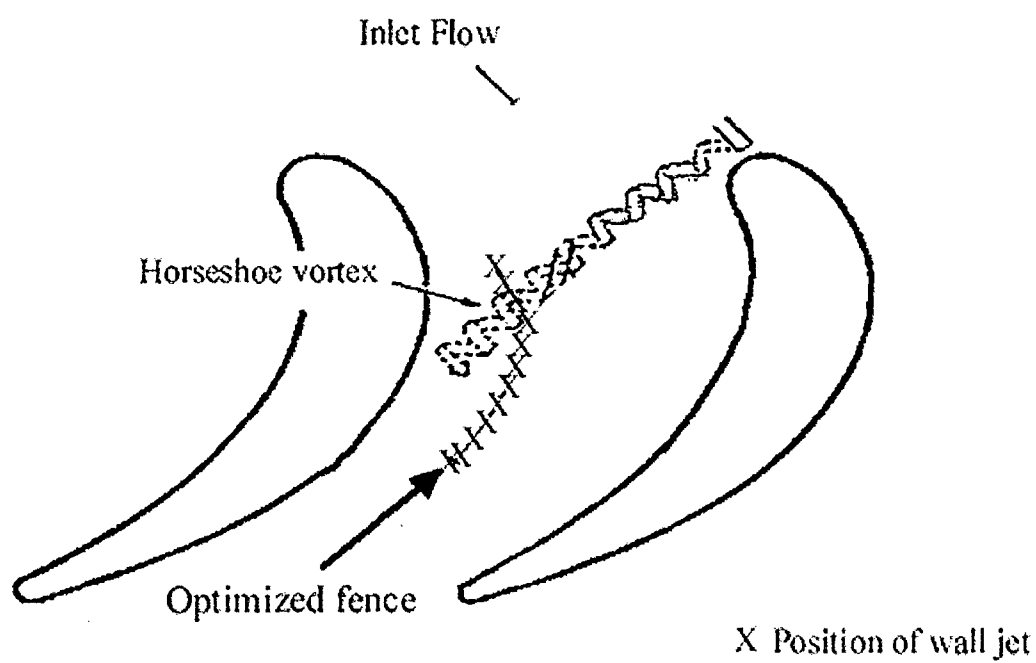


Figure 29 Top view of present text section with row of jets installed

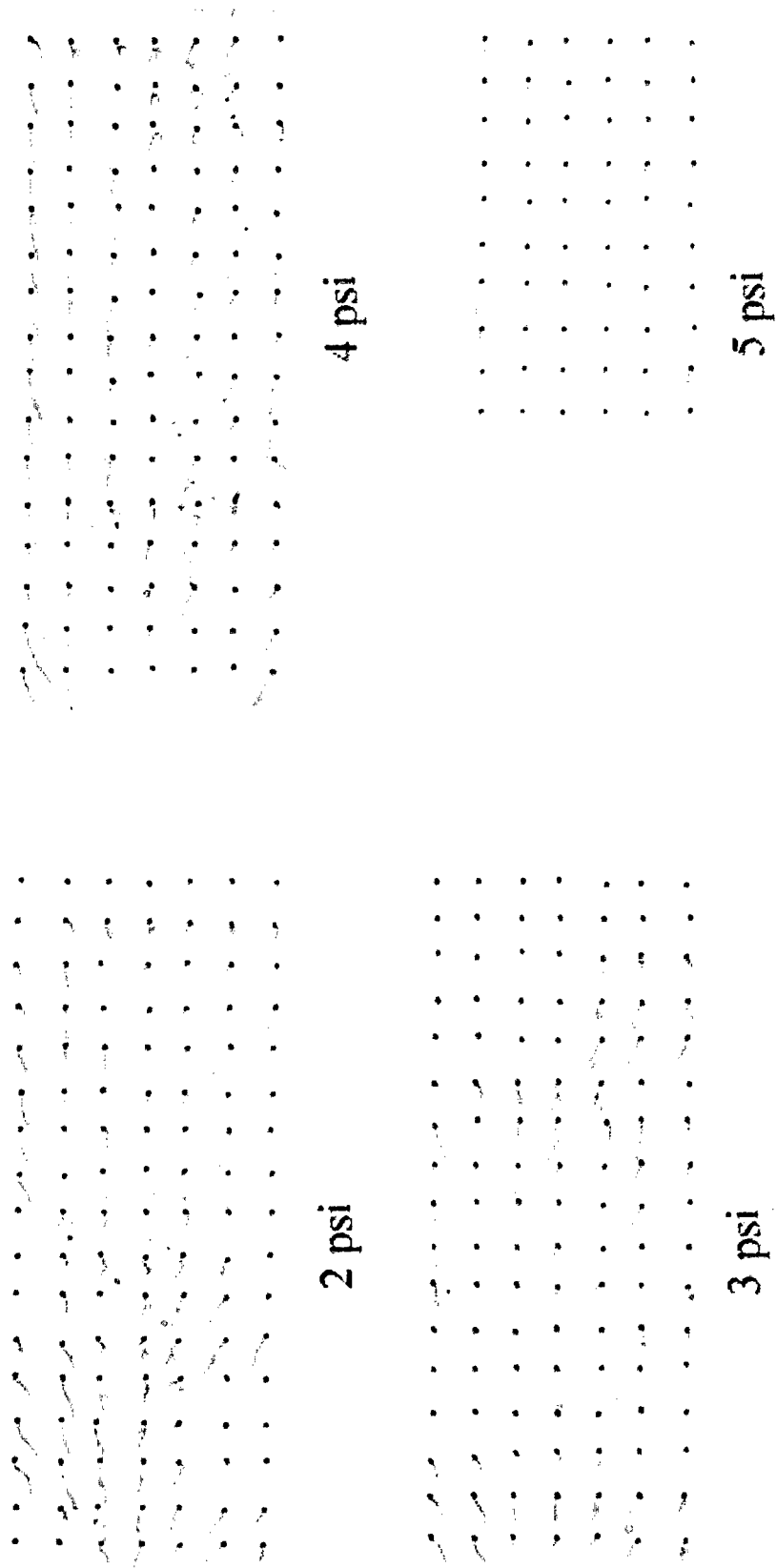
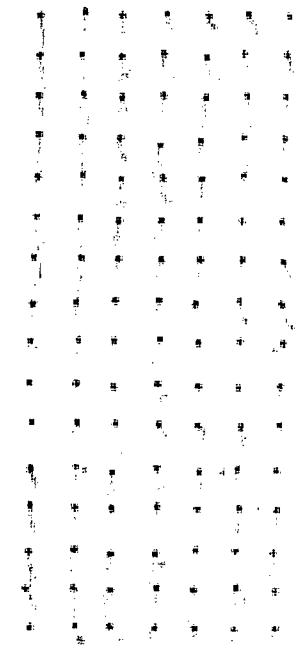
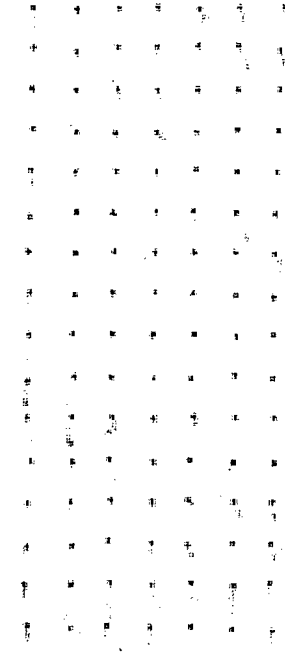


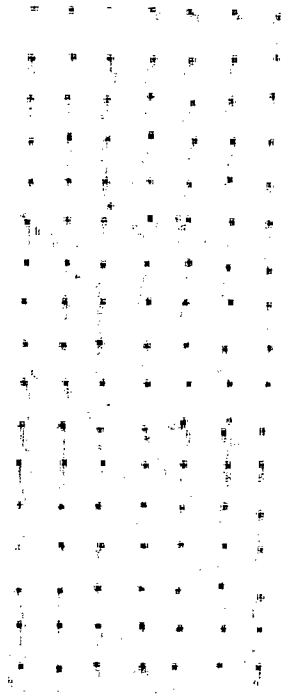
Figure 30 Ink dot flow visualization on the suction side blade



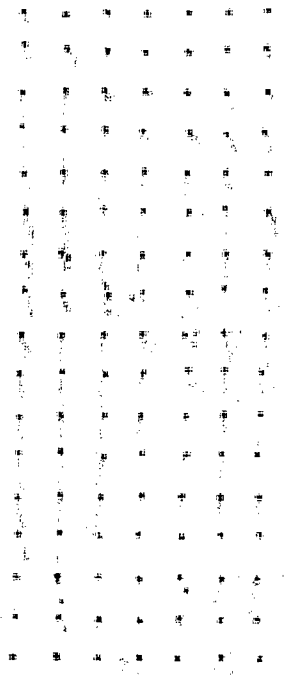
6 psi



7 psi



8 psi



10 psi

Figure 31 Ink dot flow visualization on the suction side blade

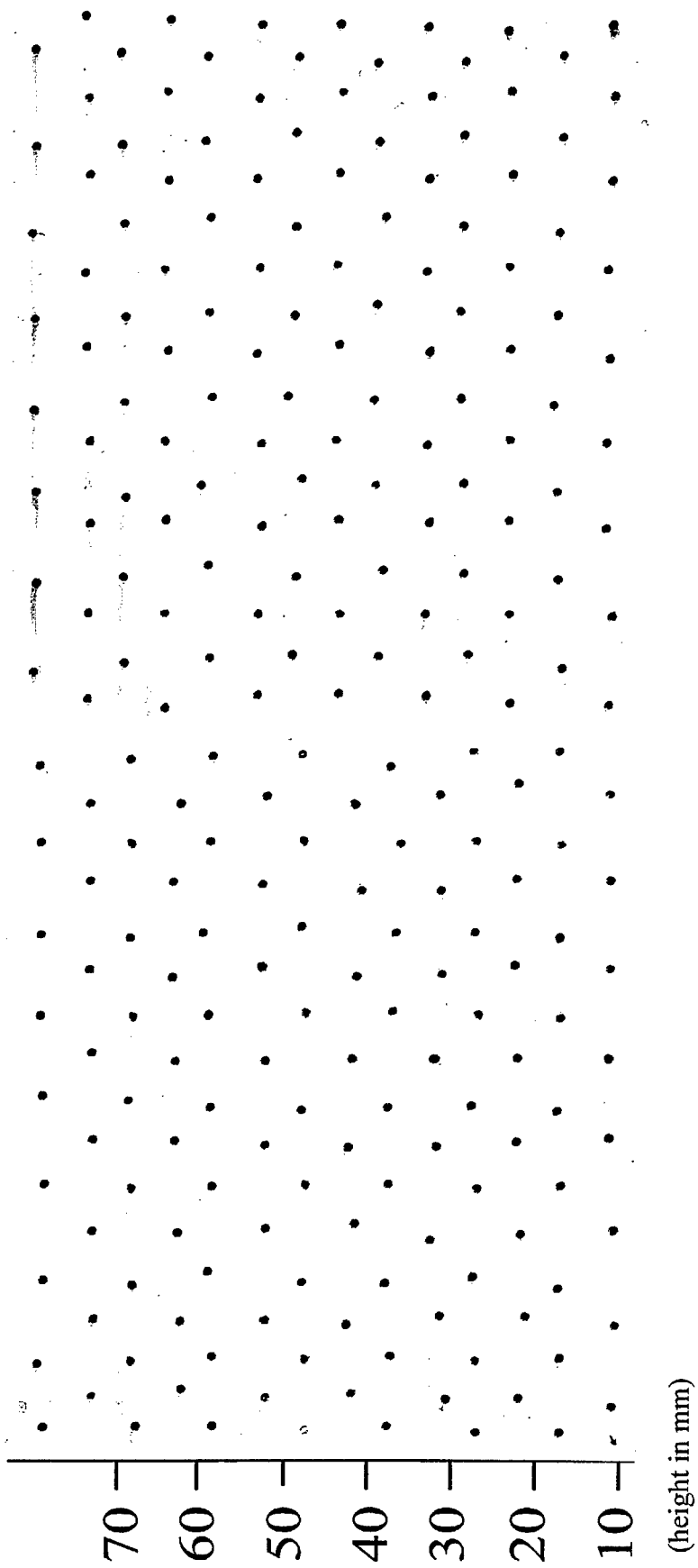


Figure 32 Ink dot visualization on the suction side blade at 7 psi

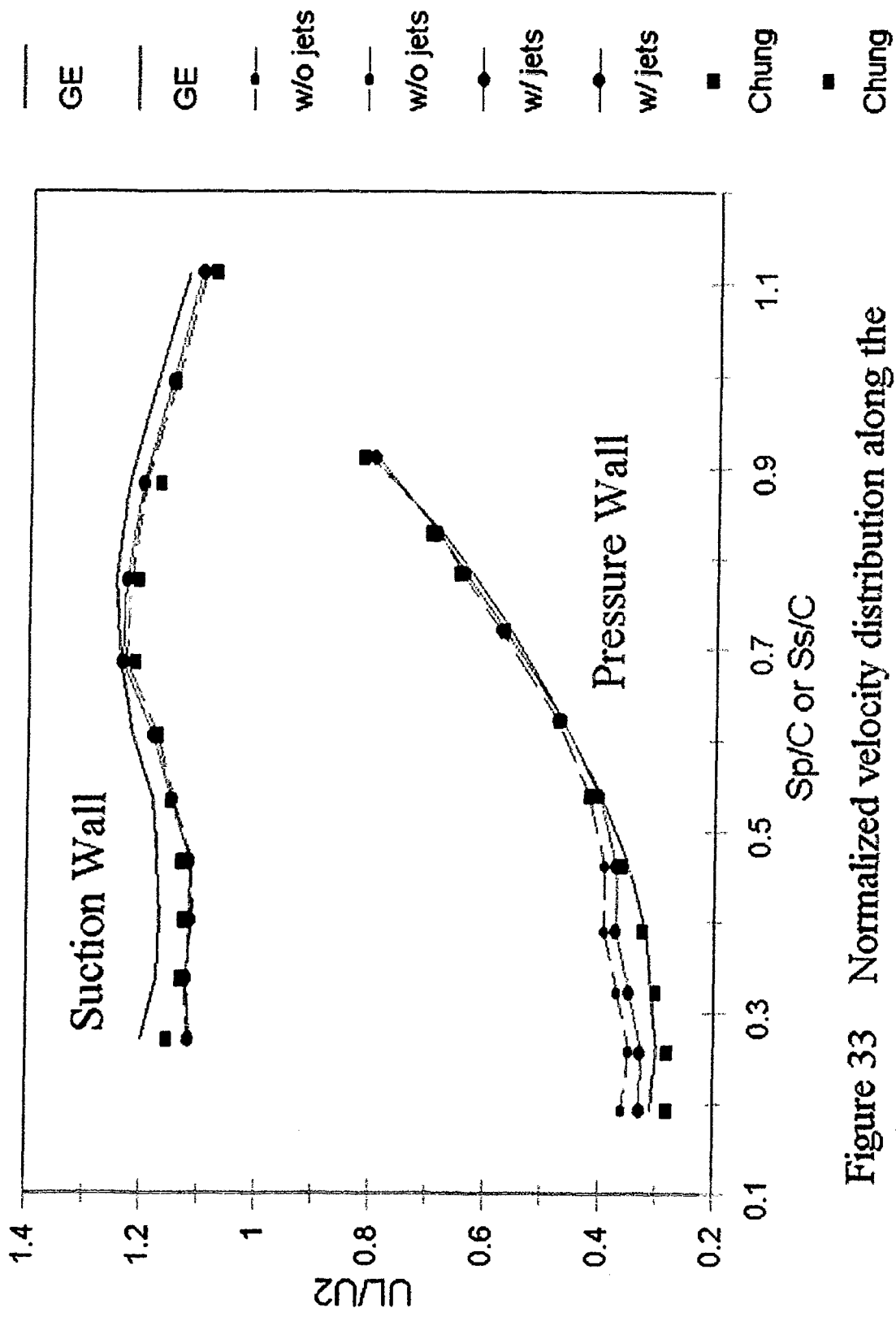


Figure 33 Normalized velocity distribution along the blade surface with wall jets at 7 psi

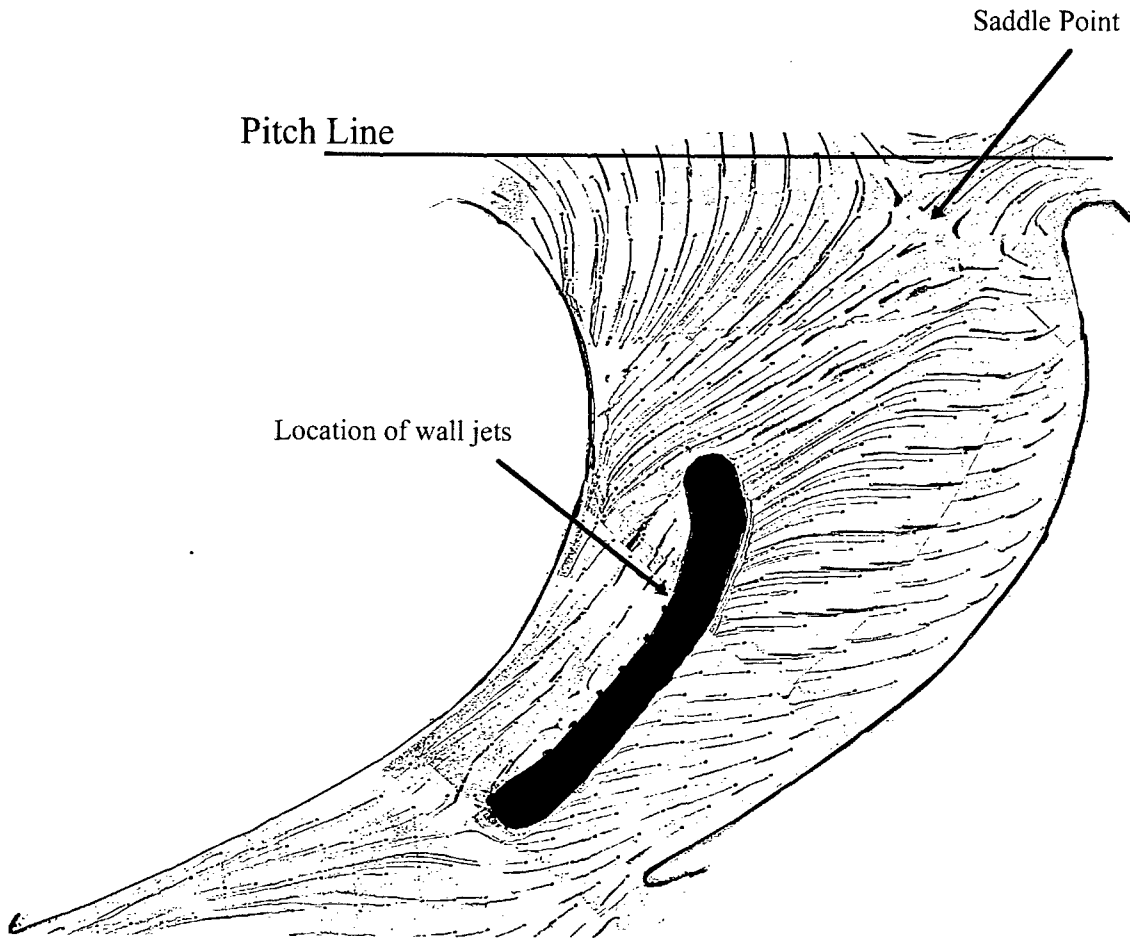


Figure 34 Ink dot traces on the endwall - with twelve jets

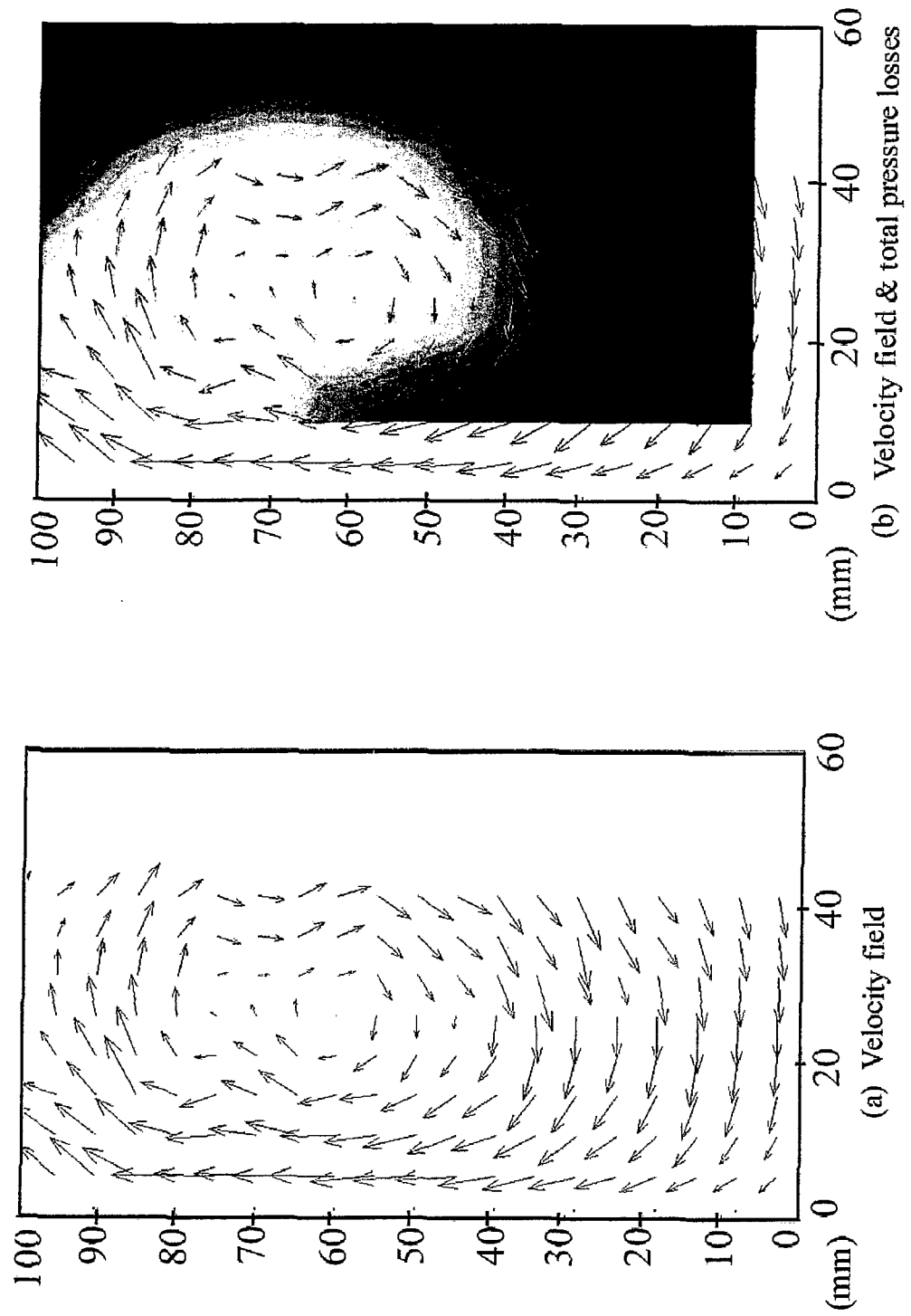


Figure 35 Velocity field and total pressure losses without jets in Plane "A"

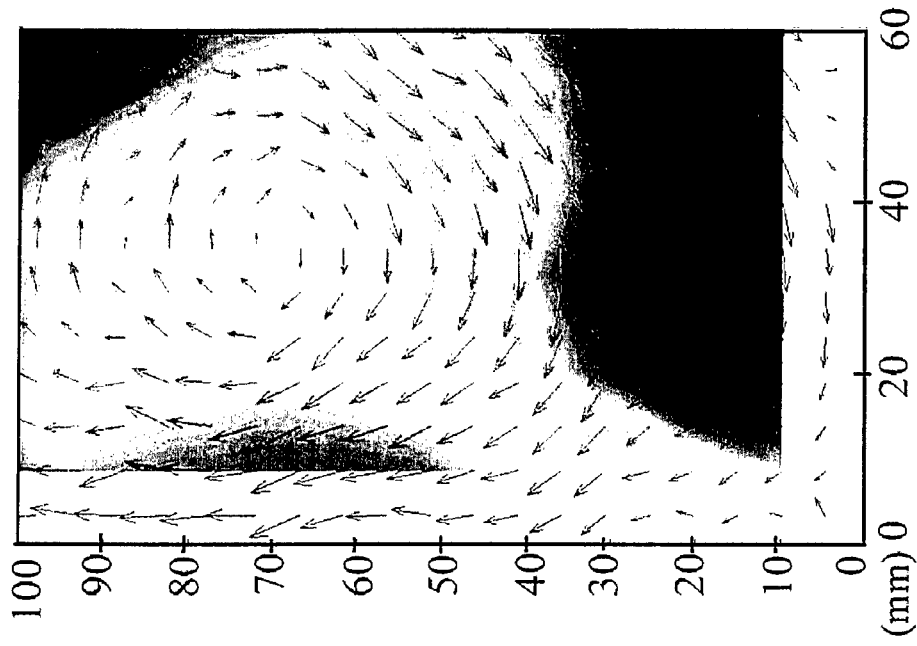
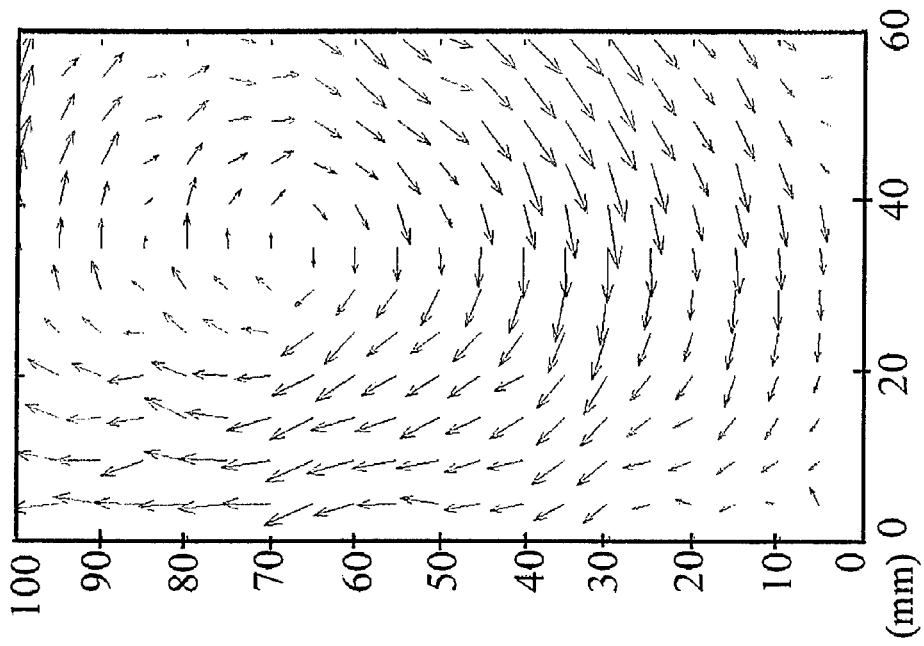


Figure 36 Velocity field and total pressure losses with jets in Plane "A"

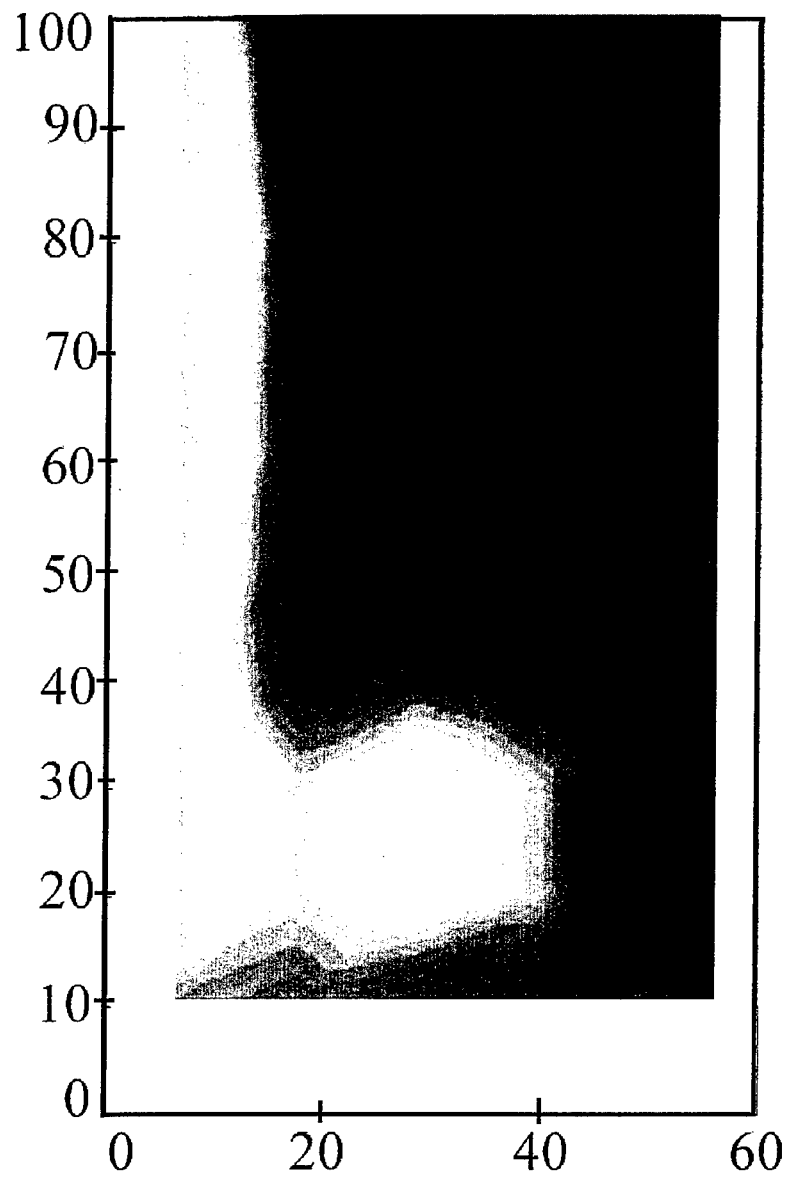


Figure 37 Total pressure losses with full fence